Extraction of weak PcP phases using the slant-stacklet transform - II: constraints on lateral variations of structure near the core-mantle boundary

Sergi Ventosa, Barbara Romanowicz

Geophysical Journal International

Geophys. J. Int. (2015) **203,** 1227–1245
GJI Seismology

doi: 10.1093/gji/ggv364

Extraction of weak *PcP* phases using the slant-stacklet transform – II: constraints on lateral variations of structure near the core–mantle boundary

Sergi Ventosa[1] and Barbara Romanowicz[1,2,3]

[1]*Departement de Sismologie, Institut de Physique du Globe de Paris, F-*75005 *Paris, France. E-mail: ventosa@ipgp.fr*
[2]*Berkeley Seismological Laboratory, University of California, Berkeley, CA* 94720*, USA*
[3]*Collège de France, F-*75231 *Paris, France*

Accepted 2015 September 2. Received 2015 August 18; in original form 2015 April 24

SUMMARY

Resolving the topography of the core–mantle boundary (CMB) and the structure and composition of the D″ region is key to improving our understanding of the interaction between the Earth's mantle and core. Observations of traveltimes and amplitudes of short-period teleseismic body waves sensitive to lowermost mantle provide essential constraints on the properties of this region. Major challenges are low signal-to-noise ratio of the target phases and interference with other mantle phases. In a previous paper (Part I), we introduced the slant-stacklet transform to enhance the signal of the core-reflected (*PcP*) phase and to isolate it from stronger signals in the coda of the *P* wave. Then we minimized a linear misfit between *P* and *PcP* waveforms to improve the quality of *PcP–P* traveltime difference measurements as compared to standard cross-correlation methods. This method significantly increases the quantity and the quality of *PcP–P* traveltime observations available for the modelling of structure near the CMB. Here we illustrate our approach in a series of regional studies of the CMB and D″ using *PcP–P* observations with unprecedented resolution from high-quality dense arrays located in North America and Japan for events with magnitude $M_w > 5.4$ and distances up to 80°. In this process, we carefully analyse various sources of errors and show that mantle heterogeneity is the most significant. We find and correct bias due to mantle heterogeneities that is as large as 1 s in traveltime, comparable to the largest lateral *PcP–P* traveltime variations observed. We illustrate the importance of accurate mantle corrections and the need for higher resolution mantle models for future studies. After optimal mantle corrections, the main signal left is relatively long wavelength in the regions sampled, except at the border of the Pacific large-low shear velocity province (LLSVP). We detect the northwest border of the Pacific LLSVP in the western Pacific from array observations in Japan, and observe higher than average *P* velocities, or depressed CMB, in Central America, and slightly lower than average *P* velocities under Alaska/western Canada.

Key words: Time-series analysis; Wavelet transform; Spatial analysis; Mantle processes; Body waves.

1 INTRODUCTION

The last few hundred kilometres at the base of the mantle represent a thermal and chemical boundary layer between the silicate mantle and the iron fluid core where important dynamic processes are taking place. The seismic properties of this region are distinct from those of the rest of the lower mantle (e.g. for recent reviews, see Lay & Garnero 2011; Lay 2015). Already in the 1960s, distinct shear and compressional velocity gradients with depth were observed, which led Bullen (1963) to name this region D″. From the long-wavelength point of view of global tomography, D″ is characterized by an increase in the rms velocity variations as one approaches the core–mantle boundary (CMB), and the presence of the two large antipodally located low shear velocity provinces (LLSVPs), centred near the equator in the Pacific and under Africa, and surrounded by a ring of fast shear wave velocities (e.g. Masters *et al.* 2000; Lekic *et al.* 2012). This long-wavelength structure contains a strong 'degree 2' component, present both in Vs and Vp models, and identified

from normal mode and traveltime data (Masters *et al.* 2000; Houser *et al.* 2008), which has led to suggestions of the possible stabilizing role of these structures for global mantle circulation (e.g. Torsvik *et al.* 2008; Dziewonski *et al.* 2010; Lekic *et al.* 2012; Greff-Lefftz & Besse 2012).

Vp models of large-scale structure in D″ have been obtained either from global mantle tomography, with constraints primarily from normal mode splitting data (Ishii & Tromp 1999, 2004), or from a combination of traveltimes of core-reflected (PcP) and core-refracted (PKP) phases (e.g. Tkalčić *et al.* 2002; Young *et al.* 2013). There are also some studies based on the dispersion of Pdiff (Sylvander *et al.* 1997; Valenzuela & Wysession 1998). In the latter studies, the *PcP* phase is referred to *P* in order to correct for upper-mantle effects.

In addition to this long-wavelength structure, there are indications of complexity at shorter wavelengths. The borders of the LLSVPs are found to be sharp (e.g. Ni & Helmberger 2001; To *et al.* 2005), with transitions over just a few hundred kilometres. There is a laterally varying discontinuity that marks the top of D″ (e.g. Lay & Helmberger 1983a; Thomas *et al.* 2002; Cobden & Thomas 2013) and evidence has been found for Ultra Low Velocity Zones (ULVZs), that is, localized and thin patches of strongly reduced Vs or Vp (e.g. Garnero & McNamara 2008; McNamara *et al.* 2010; Cottaar & Romanowicz 2012; Thorne *et al.* 2013; Jensen *et al.* 2013). There is also evidence for the presence, at least locally, of anisotropy in D″ (Vinnik *et al.* 1989; Cottaar & Romanowicz 2013; Lynner & Long 2014; Roy *et al.* 2014). However, the spectrum and distribution of short-wavelength heterogeneity in D″ is poorly known. From PKP(DF) precursor studies, it has been suggested that there is strong scattering originating in D″ at wavelengths of tens of kilometres (e.g. Cleary & Haddon 1972; Vidale & Hedlin 1998; Hedlin & Shearer 2000; Margerin 2003; Cao & Romanowicz 2007; Frost *et al.* 2013), which agrees with studies of short-period *P* diffracted waves (e.g. Bataille & Lund 1996) and ScS precursors (van der Hilst *et al.* 2007).

On the other hand, the lateral variations of CMB topography (up to 5 km peak-to-peak), which are important to constrain core–mantle coupling mechanisms, are poorly known (above degree 4) and have been the subject of vigorous debates (Creager & Jordan 1986; Morelli & Dziewonski 1987; Rodgers & Wahr 1993; Garcia & Souriau 2000; Sze & van der Hilst 2003). At long wavelengths, recent work indicates that the CMB is depressed under subduction zones around the Pacific, and elevated under the LLSVPs (e.g. Lassak *et al.* 2010; Soldati *et al.* 2012). Most studies of CMB topography rely on traveltime measurements of PcP and PKP phases (e.g. Soldati *et al.* 2012), sometimes adding normal mode splitting constraints (Soldati *et al.* 2013).

Separating the effects of D″ structure and CMB topography on compressional body-wave phases is a particularly challenging question. One of the difficulties comes from the uneven global sampling achieved by *PcP* measurements. *PcP* is a weak phase that is buried in the coda of the *P* wave and is therefore difficult to isolate from *P* reverberations originating in the crust and uppermost mantle, as well as depth phases. This restricts the distance range of useful *PcP* observations and necessitates the design of appropriate signal processing approaches.

To improve signal-to-noise ratio (SNR) and isolate weak body-wave phases, most studies routinely combine data of many spatially close stations using delay-and-sum (i.e. slant-stack) approaches. In particular, these intuitive array processing approaches are effective for the isolation of *PcP* precursors, such as the *P* wave reflected at the top of D″ (PdP) or at the top of an ULVZ (PuP) (e.g. Lay & Helmberger 1983b; Wysession *et al.* 1998; Thomas *et al.* 2002; Rost & Thomas 2010; Cobden & Thomas 2013; Frost *et al.* 2013; Thomas & Laske 2015).

The low directionality of seismometers (the amplitude pattern is the cosine of the angle from the orientation axis of the sensor to the incident axis of a wave), combined with the rather high inter-station distance (in wavelengths) of dense large-scale arrays, limits the performance of optimal (e.g. least-squares) array-processing approaches (e.g. Li *et al.* 2003; Lorenz & Boyd 2005). The approximate compact support of the waveform (the limited portion of the time and frequency domains in which it is concentrated) as well as uncertainties on the slowness of body-wave signals add additional difficulties with these approaches.

Alternative methods developed in the context of image processing have proven useful in dense and close to regular array deployments such as used, for example, in exploration geophysics. For example, in Radon transform-based methods, signals are projected to transformed domains to facilitate their enhancement and separation. In seismology, these methods are regularly used to obtain slowness slant stacks (also vespagrams) that separate signals according to their slowness and time of arrival, and to improve derived measurements such as that of polarization (Schimmel & Gallart 2003, 2004). For example, Gu & Sacchi (2009) map upper-mantle discontinuity topography from SS precursors using least-squares and high-resolution Radon transform methods.

In Ventosa & Romanowicz (2015) (from here on referred to as 'Paper I'), we introduced the slant-stacklet transform to improve SNR and to separate weak body-wave phases from other signals which, combined with coherency-guided filters, allowed us to obtain clean *PcP* observations in situations of low SNR and high signal interference. We illustrated the performance of this method in obtaining high-quality differential *PcP–P* traveltime measurements on two examples, using data from dense arrays located in North America.

Here, we present the results of application of this method to a larger data set collected from dense arrays in North America and Japan. We first briefly summarize the data processing methods to separate signals in slowness and to estimate differential traveltimes. We then discuss the main sources of bias in the obtained *PcP–P* traveltime differences and how to correct for those, when possible. In a context where the coverage and the number of events sampling an area of the CMB are extremely limited, this step is of key importance to improve the level of accuracy and confidence in the observations. We conclude by stressing the importance of mantle corrections and discussing the results in terms of what they tell us about lateral variations of structure near the CMB around the Pacific.

2 *PcP–P* TRAVELTIME DIFFERENCE ESTIMATION

The waveform of *PcP* is not only highly correlated with the waveform of *P* but also with many other close arriving phases. These signals, which are often stronger than *PcP*, can be more correlated with *P* than *PcP* itself, leading to ambiguities and misinterpretations. The most prominent signals are the p and s depth phases of *P* (pP and sP), other related phases interacting with crust and upper-mantle discontinuities and sometimes *PcP* precursors.

The strategy we follow in Paper I aims at improving *PcP–P* traveltime accuracy and extending the distance range in which these measurements can be made through, (1) isolating *PcP* (and P) to reduce interference with other correlated signals and (2) improving

the robustness of the traveltime difference estimation against uncertainties caused by close arriving signals. In order to isolate *P* and *PcP*, we introduce the slant-stacklet transform to build adaptive filters in slowness. For the traveltime difference estimation, we use two short sliding windows (as opposed to one fixed on *P* and one movable on *PcP*) to avoid contamination from other close signals (e.g., pPcP-pP) and to improve their identification.

2.1 The slant-stacklet transform and its use on slowness filters

The slant-stacklet transform decomposes the seismograms of a group of close stations (typically from an array) according to instantaneous slowness at different scales (equivalently, frequency bands). To do this expansion, we first generate a family of localized planar wavefields that span a portion of the time-space-scale-slowness domain enclosing the signals under analysis; and then, we multiply (inner product) the seismograms with every member of this family. To build this family of functions, we use a single mother function $\phi(t, x) = a(x)\psi^*(t)$, composed of a short-duration zero-mean wavelet $\psi(t)$ satisfying the admissibility condition of the wavelet transform, $C_\psi = \int_0^\infty |\hat{\psi}(\omega)|^2 \frac{\mathrm{d}\omega}{\omega} < \infty$, along the time axis, and a weighting function $a(x)$ along the space axis. We specifically write the slant-stacklet transform of a wavefield $u(t, x)$ as:

$$W v_{p,x_c}(\tau, \lambda) = \int_{-\infty}^{\infty} \int_{-\infty}^{\infty} u(t, x) \phi_{p,\lambda}(t - \tau, x - x_c)\, \mathrm{d}t\, \mathrm{d}x, \qquad (1)$$

where t is time, x is location, τ is delay and x_c is a centre location (commonly, but not necessarily, the location of a station). The family of functions writes

$$\phi_{p,\lambda}(t, x) = a_\lambda(x) \frac{1}{\sqrt{\lambda}} \psi^* \left(\frac{t - p^T x}{\lambda} \right), \qquad (2)$$

where λ is scale, $\psi^*(t)$ is the complex conjugate of $\psi(t)$ and p^T is the transpose slowness vector, to account for in-plane and out-of-plane arrivals.

Every member of this family of functions has a characteristic slowness, scale and space size. These parameters together with the mother wavelet and the weighting function control the resolution in the transformed domain. The main decisions to be made are selecting (1) the time–frequency resolution of $\psi(t)$ and (2) the space–slowness resolution that is controlled by $a(x)$ or, roughly, by the aperture of the subarray form with the group of stations used. Note that the aperture of the subarray may be a function of scale and location and, in consequence, the space-slowness resolution may change with them.

After projecting the signals to the transformed domain, we need to locate them to define appropriate filters. Conventionally, we could search for maxima of instantaneous slowness close to their expected theoretical values. This strategy is frequently problematic due to (1) the wide dynamic range of energy of seismic signals, hindering the definition of thresholds for noise attenuation and for discerning actual signals from plain noise, and (2) the possible variations in the level of noise, for example, as a result of scattering.

In order to better distinguish signals from noise, we choose to look for maxima of coherence, a measurement more closely related to the SNR with typical values of 1 when the SNR is high and close to zero when it is low. In the case of the slant-stacklet transform, this amounts to replacing the weighted sum over x, eq. (1), by a coherence estimator. In particular, we opt for coherence estimators for analytic signals, such as the phase-stack coherence estimator (Schimmel & Paulssen 1997) or estimators based on geometrically normalized cross-correlations (appendix of Taner *et al.* 1979), to improve robustness and accuracy with respect to real signal alternatives (see Paper I, section 2.4).

Once we know the instantaneous slowness location of the signals, we can design the filter and synthesize the results back to the original domain. For this purpose, we impose gains to a finite set of slownesses, and we subsequently define an inverse transformation. We specifically make a weighted sum along slowness followed by an inverse wavelet transform. Alternatively, it is possible to use more aggressive non-linear filters following Schimmel & Gallart (2007) by introducing a coherence weighted term before the inverse wavelet transform. In the following, we do not consider this term in order to preserve linearity.

The main complexity of these filtering and synthesis operations arises from the finite slowness resolution of the transformed domain. The design of a filter is trivial when signals are well separated in the transformed domain and it becomes progressively harder as signal separation reduces. Nonetheless, those signals that the slant-stacklet transform can still distinguish but cannot fully separate can be isolated, if their cross-interference is known accurately enough. We calculate these cross terms as the response of a planar wavefield to the analysis and synthesis operations. More details on the mathematical formalism and illustrations can be found in Paper I, sections 2.2, 2.3 and 3.

2.2 Traveltime difference estimation with two sliding windows

We can obtain differential traveltimes automatically as a maximum of correlation using a window fixed on *P* and one movable on *PcP*. These windows have to be long enough to include the waveform of *P* or *PcP* but as short as possible to reduce noise and interference from other correlated signals. However, the higher uncertainties on absolute arrival times than on differential arrival times together with the strong variations in the signal duration and in the interfering signals hinders the optimal location and length of these windows.

We allow for shorter windows by introducing two sliding windows the position of which is controlled by two delay parameters, one for the absolute position of the window along *P*, t_a, and another for the differential position between *P* and *PcP*, t_d. We specifically use the following objective function:

$$\max_{t_a, t_d} \frac{|\langle x_1(t - t_a), x_2(t - t_d - t_a)\rangle|^2}{\|x_1(t - t_a)\|^2}, \qquad (3)$$

where $\langle x_1(t), x_2(t)\rangle$ defines the (windowed) inner product between x_1 and x_2. Then $\langle x_1(t - t_a), x_2(t - t_d - t_a)\rangle$ is its (windowed) cross-correlation. In this function, we replace the standard criterion of maximum of correlation by a maximum of energy reduction on the candidate *PcP* signal, x_2, using the *P* signal, x_1, seeking for a better balance between waveform similarity and energy. More details can be found in Paper I section 4.

2.3 Application to *PcP–P* traveltime differences

Fig. 1(a) shows raw velocity time-series for a deep earthquake in northern Chile observed in North America at stations with good quality signal selected from the IRIS database (Fig. 1b). We can clearly distinguish the *P* wave and, about 30 and 40 s later, pP and sP. Much weaker, *PcP* is hard to observe owing to its low SNR and to interference with much stronger pP, sP and later arriving phases.

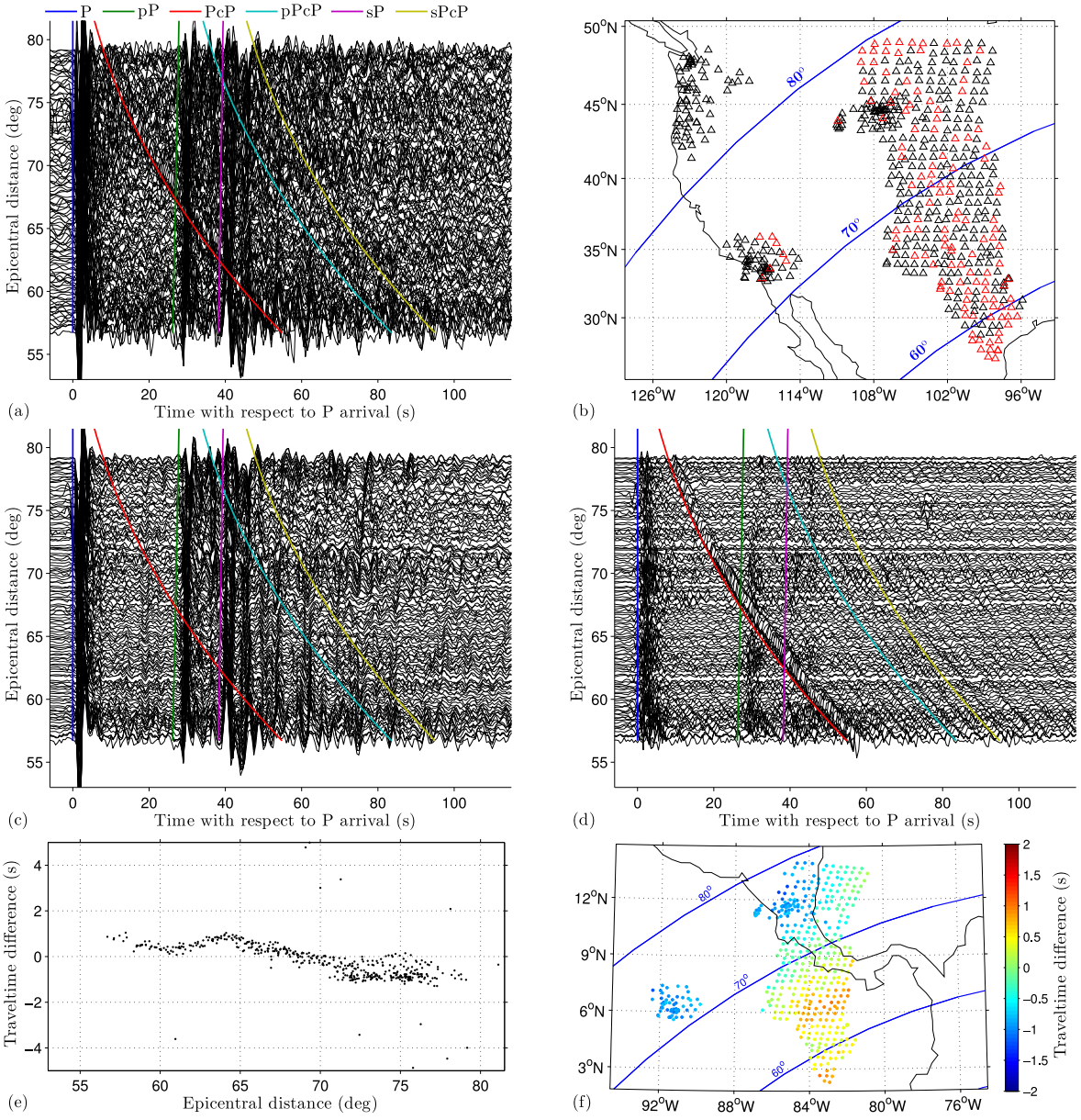

Figure 1. Illustration of the estimation of *PcP–P* traveltime anomalies. (a) Velocity record section for an earthquake in northern Chile (2010/03/04 22:39:26.5 UTC, $M_w = 6.3$, depth = 114 km) observed on USArray. Instrument response has been removed, data are bandpass filtered from 1 to 60 s and seismograms are aligned on the measured arrival time of the *P* wave. (b) Epicentral distances (blue lines) and location of the stations with good quality signal shown in (a) (red triangles) and those not shown (black triangles) for clarity. (c) *P* and (d) *PcP* extractions from the data shown in (a) with the same amplitude normalization. Measured *PcP–P* traveltime differences compared to AK135 1-D model, $(PcP–P)_{data} - (PcP–P)_{model}$ at all the stations; (e) sorted by epicentral distance and (f) mapped to the reflection points of *PcP* at the CMB (here measurements outside of the ±2 s range are interpreted as outliers).

We extract *P* (Fig. 1c) and *PcP* (Fig. 1d) from the raw data (Fig. 1a) using the slant-stacklet transform with the configuration used in the examples shown in Paper I section 3 to filter raw data in slowness. In particular, in the analysis operation, $a(x)$ is a uniform weighting function, $\psi(t)$ is the complex Morlet wavelet and the aperture of the subarrays is 0.33 deg s^{-1}, with a minimum value of 2° and a maximum one of 6.7°, in a period range of 1 s to about 54 s. In the filtered traces, we search for in-plane coherence maxima for both *P* and *PcP* in a wide slowness range around 1-D model predictions, and we use the minimum noise solution on the synthesis operation. Now, in Fig. 1(d), we can clearly identify and follow *PcP* with epicentral distance. Only small remainders of pP and sP signals, much lower than *PcP*, can be seen.

The higher SNR and better signal separation achieved in Figs 1(c) and (d) dramatically improve the quality of traveltime difference estimations. Figs 1(e) and (f) show the traveltime measurements obtained using the method of the two sliding windows with the maximum energy reduction criterium, eq. (3). This method helps to further reduce bias and outliers with respect to the standard cross-correlation method.

3 SOURCES OF BIAS IN *PcP–P* TRAVELTIME DIFFERENCES

The accuracy of *PcP–P* traveltime differences is limited by the highest frequency of the signals used and the level of noise

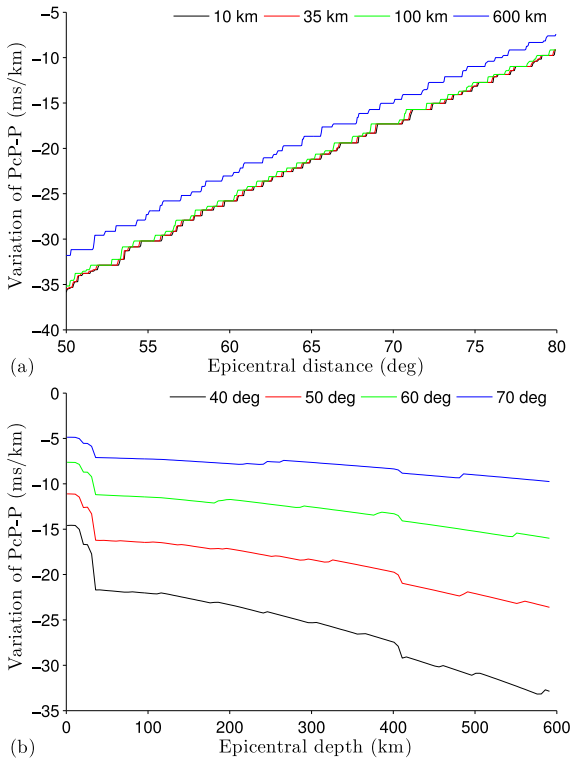

Figure 2. Differential *PcP–P* traveltime bias per km of (a) epicentre mislocation at four epicentral depths and (b) depth difference for epicentral distances of 40° to 70°.

and interferences (coherent noise). These observations may contain additional biases due to a combination of external factors. *A priori*, the main sources of bias are mantle heterogeneities, earthquake mislocation, intrinsic attenuation and wave-propagation approximations.

The International Seismological Center (ISC) Bulletin provides high-quality hypocentre reports. Bondár & Storchak (2011) show cumulative distributions of mislocation and depth differences from ground truth for several location algorithms. About 90 per cent of the earthquakes with free-depth solutions have mislocation and depth differences less than 10 km. This reduces to 2.5 km mislocation and 4 km depth difference for 50 per cent of them. These errors introduce a bias on *PcP–P* traveltimes that varies according to epicentral distance and depth. The bias due to mislocation (Fig. 2a) reduces as epicentral distance and depth increase; while the bias due to depth difference (Fig. 2b) grows as focal depth increases and epicentral distance decreases. For example, when an earthquake with reported epicentral distance of 60° and depth of 100 km is actually 5 km farther away, *PcP–P* will have a bias of −0.129 s; whereas if it is 5 km shallower than predicted, the bias will be +0.058 s.

Most earthquakes with magnitudes $M_w < 5.5$, and sometimes even larger, are too noisy for accurate *PcP–P* analysis. Epicentral locations of larger magnitude earthquakes are good enough to safely ignore any bias introduced by mislocation or depth difference (below 0.1 s typically) because (1) it is typically below the actual accuracy of *PcP–P* observations, and (2) the bias introduced by mantle heterogeneities is much higher. The bias introduced by intrinsic attenuation and anisotropy are typically lower than that caused by epicentre estimation errors. Despite it being small, we do correct for intrinsic attenuation using the 1-D QL6 model (Durek & Ekström 1995). Even severe and localized intrinsic attenuation heterogeneities with a very low Q extending from the asthenosphere to the bottom of the upper mantle would introduce biases that are difficult to observe at high frequencies, mainly due to their impact on relatively small and shallow portions of the *PcP–P* sensitivity kernel with little weight on the overall traveltime difference. Because of similar reasons, we consider bias due to anisotropy negligible. Among the sources of bias we discuss, earthquake mislocation and intrinsic attenuation are negligible compared to mantle heterogeneities.

The main purpose of referring *PcP* observations to *P* is to reduce contributions to traveltimes from regions with strong heterogeneities outside D″ as well as uncertainties on source parameters among other sources of bias. In view of the Fresnel volumes of *P* and *PcP*, this is especially useful for correcting for effects of the crust and of the top of the upper mantle for large epicentral distances, where *P* and *PcP* have closer travel paths.

The separation of *P* and *PcP* travel paths (Fig. A1) is approximately proportional to depth in their shallow portions and progressively increases as the epicentral distance decreases. Meanwhile, the radius of the Fresnel volumes increases roughly as the square root of the minimum wavelength and the inverse of the sum of the inverses of the travel distance to the source and the station. This greatly reduces the sensitivity of *PcP–P* traveltime differences to mantle heterogeneities at shallow depths and large epicentral distances where P and *PcP* kernels mostly overlap. However, the sensitivity is still large in the transition zone for short epicentral distances or short wavelengths, and at larger depths, where the kernels do not overlap. An example showing the bias due to mantle heterogeneities and variations in the Moho and the 670 discontinuity depth is shown in the Appendix.

Approximations of wave propagation theory considered in the computation of reference traveltimes using 1-D/3-D models, may introduce additional bias. The most accurate solution is computing synthetic seismograms solving the full wave equation on global 3-D models to obtain traveltime differences as a delay between synthetic and observed waveforms. At long periods, these forward problems are routinely solved in a high performance computer environment, but their poor scaling towards shorter periods makes them numerically intractable at the present time. To make these problems more tractable, we can (1) use simpler models or (2) make approximations on the wave equation. The direct solution (Kawai *et al.* 2006) and the axi-symmetric (Nissen-Meyer *et al.* 2014) methods define tractable (still demanding) forward problems using the full wave equation up to 2 Hz in 1-D and 2-D models, respectively. For *PcP–P* traveltime difference estimation, we need global 3-D models to account for biases due to mantle heterogeneities or structures such as slabs and upper-mantle discontinuities. Infinite frequency approximations (i.e. ray tracing) are still the most commonly used alternative to calculate traveltimes at short periods, because they are fast enough to deal with the big volumes of data, taking into account global 3-D models. The main differences among them arise from the method used for ray tracing. The ray can be traced in a reference 1-D model or, more accurately, in the 3-D model using, for example, ray shooting or ray bending methods (e.g. Julian & Gubbins 1977; Moser 1991; Zhao *et al.* 1992). We opt for the simplest option because (1) at short periods, global 3-D mantle models still have low resolution and are smooth, and (2) the epicentral distances we consider are relatively large. This approximation introduces an error that is much smaller than the actual mantle corrections calculated with the current mantle models. Eventually, as higher resolution models become available 3-D ray tracing may need to be considered.

We illustrate in the next section the importance of employing accurate global 3-D mantle models to correct for mantle heterogeneities.

4 CORRECTIONS FOR MANTLE HETEROGENEITIES

We consider available global 3-D Vp models to correct for mantle heterogeneities. While Vp models have higher resolution under sources (often close to subduction zones) and receivers (mostly on land), Vs models have more uniform global resolution (in particular under oceans). Since differential traveltimes are not sensitive to the crust and uppermost mantle, we therefore also consider Vs models, and convert to P velocity using the ratio $R = \mathrm{d}\ln V_s/\mathrm{d}\ln V_p$. $R \sim 1.7$ in the upper mantle and the mid mantle may increase to $R > 3$ in the lowermost mantle but its value is not very well constrained (e.g. Masters *et al.* 2000; Romanowicz 2001; Samuel *et al.* 2005; Brodholt *et al.* 2007). There are also depth and lateral variations located in the crust and the uppermost and lowermost mantle.

Fig. 3 shows vertical cross-sections of Vp in the mantle along a great circle path (solid red line in Fig. 3a) for the example of an event sampling the CMB at the gulf of Alaska developed in figs 1, 3 and 8 of Paper I. In this example, a local maximum in the differential traveltime is clearly visible in the middle of the D″ region sampled (red colour in Fig. 3a). The question is whether to attribute this sharp and localized maximum to a heterogeneity in D″, versus somewhere in the mantle, or a combination of both. First of all, the width of this maximum is four times smaller than the Fresnel zone radius at the CMB at 2 s in the great circle plane (about 8° for epicentral distances of 60° to 70°). Second, when we compare the time of arrival of P and PcP with respect to their predictions (Paper I Figs 3a and c), we can appreciate that, while PcP arrival times remain relatively constant as a function of epicentral distance, P arrival times vary significantly. In particular, P is faster than average at epicentral distances of about 65°–70°. This indicates that this traveltime difference anomaly must be due to a heterogeneity extending along the P kernels. Considering the radius of the Fresnel zone and the separation of the rays in this distance range (Fig. A1), this heterogeneity should be deeper than 300 km.

The dynamic range of Vp variations in the transition zone and the lower mantle is about 1 per cent in global Vp models, and slightly higher is some regional models. Figs 3(b) and (d) show Vp variations along this cross-section in models MIT-P08 (Li *et al.* 2008) and LLNL-G3Dv3 (Simmons *et al.* 2012), respectively, and Figs 3(f) and (h) Vs variations from SEMUCB-WM1 (French & Romanowicz 2014) and S40RTS (Ritsema *et al.* 2011). Solid black lines are P and PcP ray paths departing from the source to several receivers located at epicentral distances of 60°–70°. These ray paths progressively separate with increasing epicentral distance. Therefore, heterogeneities on the source side introduce bias on traveltimes which project to wider areas of the CMB than heterogeneities on the receiver side.

In order to explain this traveltime anomaly, we then search for a heterogeneity in the transition zone and/or the upper lower mantle on the receiver side along the Fresnel volume of P at epicentral distances of about 65°–70°. This heterogeneity should affect a significant portion of the path according to the expected low Vp variations. When we check the models carefully, we see that all of them report a high velocity zone (in blue) centred along the P ray path for stations at epicentral distances of 68° from depths of about 660 km to about 1500 km or deeper (western Pacific subduction zone), and a close to zero velocity variation along PcP for the same stations and depth interval. They however disagree on the particular shape of this anomaly. This heterogeneity is located across the P rays paths of 66°, 68° and 70° (see, e.g. Fig. 3d), which fully match with the location of the maximum of traveltime difference in Fig. 3(a). The LLNL-G3Dv3 model shows d lnVp of 0.5 to 1 per cent from 660 to about 1700 km, which is more than sufficient to explain observations in Fig. 3(a). MIT-P08 shows slightly lower but smoother d lnVp variations with a similar extension in depth. The SEMUCB-WM1 and S40RTS models, smoother than the Vp models in this area, shows d lnVs up to 1 per cent for about the same depth range.

Figs 3(c), (e), (g) and (i) show mantle corrections according to these 4 global models, respectively, using the approximated ray paths of AK135 1-D model and a R conversion factor of 2 for SEMUCB-WM1, and one that increases with depth from 1.25 at the surface to 3 at the CMB for S40RTS (Ritsema & van Heijst 2002). These values of R were used for the construction of these models. We explored the possibility of refining the values of R, however we found that with the data sets available, we could not constrain it significantly better. In these corrections, we exclude the lowermost mantle (>2500 km) to make PcP–P constraints on D″ relative to a global 1-D model, and the shallowest part of the upper mantle (<100 km) because of the large overlap of the sensitivity kernels. We see, in these figures, that most models agree on the maximum bias due to mantle heterogeneities, up to ±1 s for this particular example. Nevertheless, models disagree on the details of mantle corrections.

All models agree on the general trend of the mantle corrections along the coast of the gulf of Alaska. They suggest positive corrections in the west of 143°W meridian and negative or close zero in the east, but their mean and the sharpness of their main features differ. LLNL-G3Dv3 gives stronger mantle corrections than MIT-P08, as predicted from the relative strength of these models. The mantle corrections from Vs models are smoother than for Vp models and, in this example, larger (more positive) than the ones from Vp models. This is explained by the relatively weaker velocity variations of Vs models in the mid-mantle along the P and PcP Fresnel volumes (e.g. follow the P ray path of 68° from about 660 km depth at the receiver side). Comparing these corrections with the observations shown in Fig. 3(a), we see that Vp models are better able, in this example, to remove the strong local lateral variations observed in the raw data.

Fig. 4 shows observations before and after applying mantle corrections using the above models. Comparing Figs 4(a) and (c), we see that most of the short-wavelength oscillations in traveltime anomalies disappear when using LLNL-G3Dv3, and in particular, the maximum (in red) caused by the slab. After correction, observations are smooth, in agreement with the Fresnel zone resolution of PcP at CMB, with a mean value close to zero. A few relatively sharp oscillations appear in the southeast part of Fig. 4(c) that may be caused by residual mantle heterogeneities, the roughness of LLNL-G3Dv3, or due to approximation of wave propagation by rays traced in 1-D models. The MIT-P08 model (Fig. 4b) does not fully remove the contamination from the slab, but it introduces weaker perturbations than LLNL-G3Dv3 (e.g. compare the southeast part of Figs 4b and c). The two Vs models (Figs 4d and e) perform similarly, they increase slightly the mean of the traveltime differences and achieve a minor reduction of the contamination from the slab. In summary, mantle corrections are clearly important, but differ in detail from model to model. A possible objective criterion to evaluate results after mantle corrections is variance reduction, other more subjective

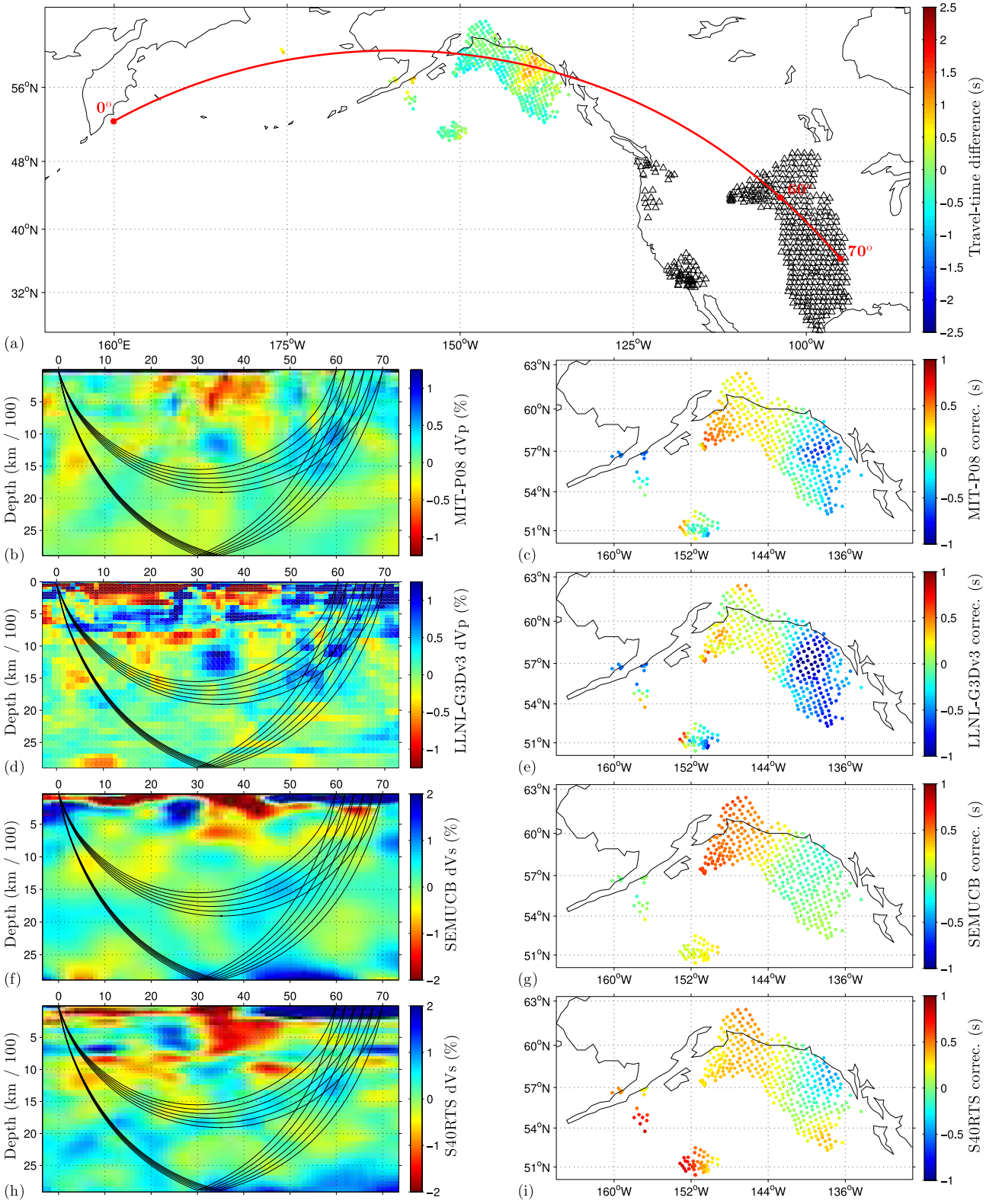

Figure 3. Contributions of mantle heterogeneities to the *PcP–P* traveltime anomalies for an earthquake off the east coast of Kamchatka (2010/07/30 3:56:19.2 UTC, $M_w = 6.3$, depth = 30.3 km) shown in Fig. 8(c) of Paper I. (a) Observed traveltime anomalies: $(PcP–P)_{data} - (PcP–P)_{model}$, mapped at the CMB in colour. Black triangles indicate stations and, in red, a great circle path from the epicentre to a station at 70°. Depth cross-sections of relative velocity anomalies along the great circle path shown in (a) for global *P* models: (b) MIT-P08 and (d) LLNL-G3Dv3, and global *S* models: (f) SEMUCB-WM1 and (h) S40RTS. Black lines are *P* and *PcP* ray paths from the source to receivers for epicentral distances of 60°–70°. Corresponding mantle corrections for *PcP–P* traveltimes, according to (c) MIT-P08, (e) LLNL-G3Dv3, (g) SEMUCB-WM1 with $R = 2$ and (i) S40RTS $R = 1.25 + 1.75z/2891.5$, where z is depth in km.

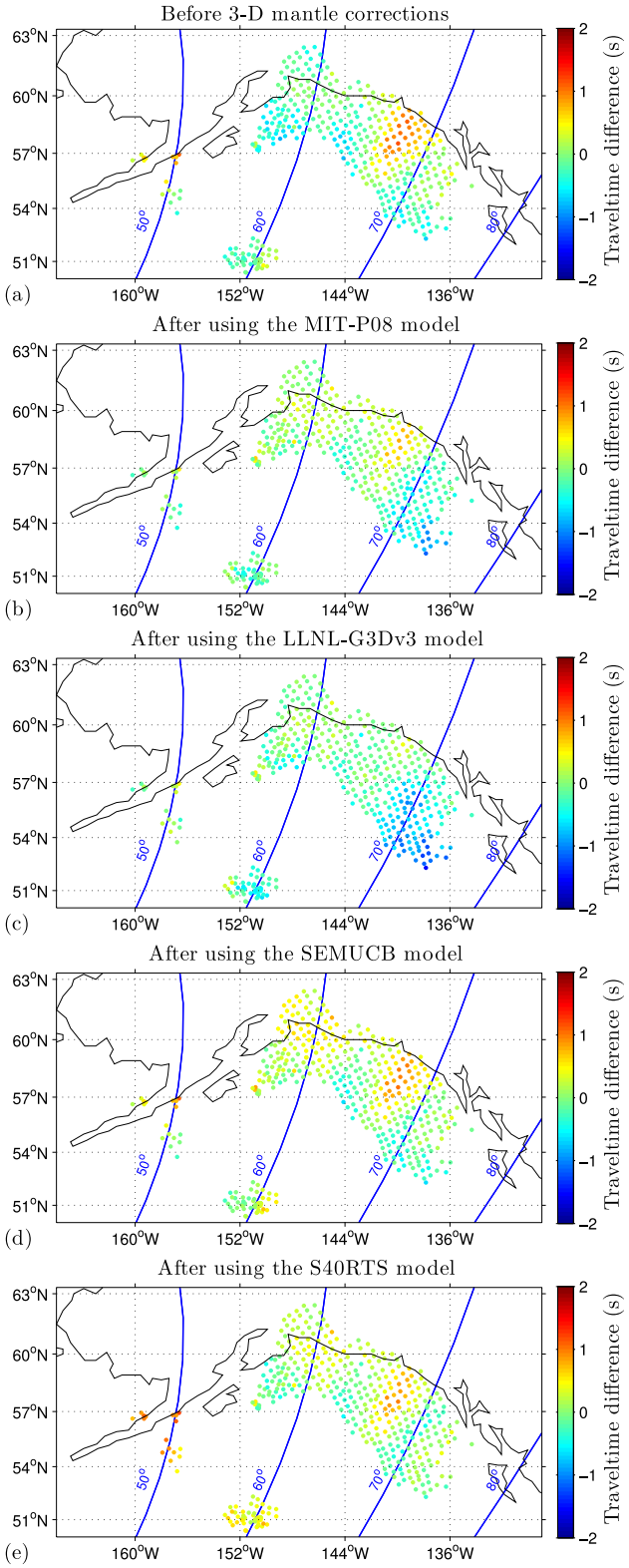

Figure 4. Observed *PcP–P* traveltime anomalies mapped at CMB for the earthquake shown in Fig. 3 (a) before, and (b–e) after mantle corrections using (b) MIT-P08, (c) LLNL-G3Dv3, (d) SEMUCB-WM1 and (e) S40RTS global models. Blue lines indicate the *PcP* reflection points for epicentral distances of 50°–80°.

criterion such as the wavelengths of the main structures are also of help.

5 REGIONAL CONSTRAINTS ON LATERAL VARIATIONS OF STRUCTURE

We now illustrate our approach by applying it to regional studies in Central America, the western Pacific and Alaska/Canada, the first two close to the Pacific LLSVP and the third one farther from it, using events with magnitude $M_w > 5.4$ and distances up to 80°. According to CMB topography studies, at large wavelengths, the CMB is depressed in Central America, Alaska/Canada regions, while in the western Pacific it is elevated (e.g. Lassak *et al.* 2010; Soldati *et al.* 2012). According to global velocity models (Fig. 11), Vp is slightly higher than average in Central America, it is much lower in the portion of the LLSVP sampled in the western Pacific region, and has close to no variations in Alaska/Canada. In contrast, Vs is much higher than average in Central America and slightly higher in Alaska/Canada.

As in the example shown in Fig. 1, we define many overlapping subarrays using stations from USArray and other nearby networks in North America, and from Hi-Net (Okada *et al.* 2004; Obara *et al.* 2005) in Japan. We use the same parameters for the *P* and *PcP* separation and for the *PcP–P* traveltime difference measurement in the three regions considered, although we could attain slightly shorter periods with Hi-Net due to its higher density. In these examples, we exclude events at distances below 42° (bottoming of *P* shallower than 1000 km) because the greater contribution of upper-mantle heterogeneities on *P* traveltimes and the large separation between *P* and *PcP* Fresnel volumes reduce the accuracy of *PcP–P* traveltime differences too much, even after mantle corrections, considering that the expected anomalies in *PcP–P* with respect to 1-D reference model should not exceed ±2 s. We evaluate the results after mantle corrections for each model individually, according to local smoothness and standard deviation of the corrected observations, and we interpret the robustness of the results according to the agreement between them.

PcP–P traveltime differences vary as a function of the *PcP* incidence angle at the CMB (according to AK135, at epicentral distances of 50°, 60° and 70° and a focal depth of 0 km, this difference is 55.5°, 64.2° and 71.8°, respectively). In order to combine data from stations at different epicentral distances sampling the same location of the CMB, we project the *PcP–P* traveltime difference with respect to the AK135 1-D model to the vertical part of the path using this angle. Assuming lateral variations small, this observation is sensitive to the vertical velocity structure of the D″ layer (about –2.7 per cent per second of traveltime difference considering a D″ of 250 km thickness) and the elevation of the CMB boundary (about −6.8 km per second of traveltime difference) and therefore it is convenient to merge data from many earthquakes. Still we cannot resolve the relative contributions of velocity and topography on the resulting traveltimes. Complementary observations, such as PKP traveltime data (e.g. Morelli & Dziewonski 1987), Pdiff traveltimes (e.g. Wysession 1996) or *PcP*/P amplitude ratios sensitive primarily to velocity, are needed to resolve this trade-off. Note that minor sources of bias for *PcP–P* traveltime differences may become significant in these observations, such as focusing effects on amplitude ratios.

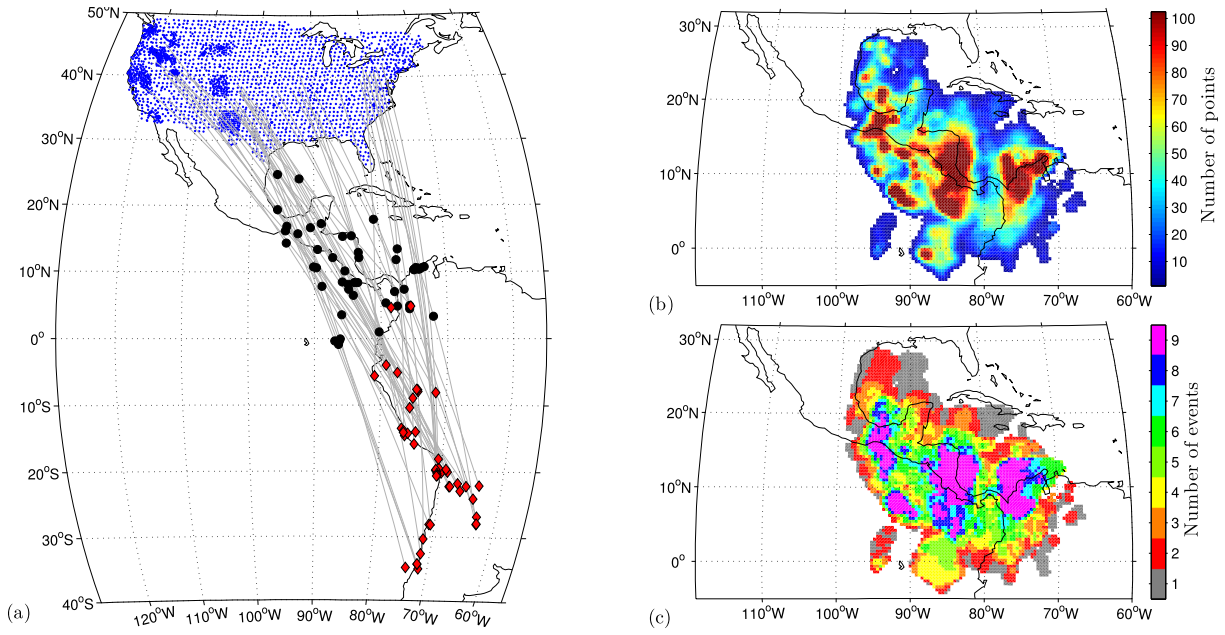

Figure 5. Data set for Central America. (a) Bounce points at the CMB (black circles) for earthquakes in South America (red diamonds) recorded in North America (blue points). Only bounce points corresponding to the centre of USArray are shown. (b) Number of stations and (c) number of events sampling the CMB within a distance of 0.7°.

5.1 Central America

Fig. 5 shows the coverage obtained in Central America from 47 earthquakes located in South America (Table 1) with a total of 18 301 high-quality *PcP* observations recorded on broadband stations in North America. Here, we have rejected outliers and stations at azimuths where the radiation of *P* or *PcP* is small or with opposite signs. Also, we have excluded 16 additional earthquakes with clear *P* signals but very subtle or undetectable *PcP* signals even after processing.

Fig. 6(a) presents local means of vertical *PcP–P* traveltime differences (after correcting for epicentral distance) with respect to AK135 1-D model and Fig. 6(b) shows their standard deviation. These results show lower than average differential traveltimes except in a band of higher values at about 80°W, with peak to peak variation of 0.9 s, much larger than the maximum standard deviation of about 0.25 s. The standard deviation has slightly stronger short wavelengths than the mean due to lateral variations in the coverage (see Figs 5b and c), and to a lesser extent, due to rapid variations in

Table 1. Event database in Central America from the reviewed ISC bulletin up to December 2012 and from the NEIC global earthquake bulletin afterwards.

Date	Time	Lat (°)	Lon (°)	Depth (km)	M_w	Date	Time	Lat (°)	Lon (°)	Depth (km)	M_w
2006-10-20	10:48:57.80	−13.4967	−76.6679	34.3	6.6	2010-10-21	02:49:55.93	−34.7602	−73.8125	9.2	5.8
2007-03-18	02:11:07.56	4.6445	−78.4592	17.7	6.1	2011-01-01	09:56:58.46	−26.8513	−63.2373	584.3	7.0
2007-07-12	05:23:49.70	−7.9279	−74.3249	152.4	6.0	2011-04-02	10:59:39.10	−19.6717	−69.2191	102.0	5.9
2007-07-21	15:34:52.91	−22.2136	−65.7495	290.6	6.3	2011-08-24	17:46:11.56	−7.6203	−74.5380	149.3	7.0
2007-08-18	02:52:36.11	−13.8095	−76.2970	33.4	6.0	2011-10-06	11:12:30.00	−24.1315	−64.2963	16.5	5.9
2007-09-26	04:43:18.01	−3.9580	−79.2174	102.1	5.9	2011-10-28	18:54:34.75	−14.5572	−76.1207	29.0	6.8
2008-02-04	17:01:31.28	−20.1855	−69.9476	42.8	6.3	2012-01-30	05:10:59.46	−14.2139	−75.6584	34.2	6.3
2008-03-24	20:39:07.96	−20.0782	−68.9726	120.8	6.2	2012-04-17	03:50:15.28	−32.6374	−71.5641	29.7	6.6
2008-07-01	00:17:32.78	−10.3573	−75.5019	28.5	5.4	2012-05-28	05:07:23.52	−28.0210	−63.1134	591.1	6.7
2008-08-26	21:00:36.74	−7.6632	−74.3692	153.9	6.4	2012-06-02	07:52:54.60	−22.1017	−63.6574	539.4	5.9
2008-09-13	09:32:02.13	4.8429	−75.4786	133.7	5.7	2012-11-10	14:57:50.21	−8.9367	−75.0884	128.6	6.0
2009-07-14	18:38:08.33	−21.8184	−67.1280	175.7	5.7	2013-01-30	20:15:43.30	−28.0900	−70.6500	45.0	6.8
2009-11-13	03:05:58.31	−19.4690	−70.4181	36.0	6.5	2013-02-22	12:01:58.20	−27.9300	−63.1000	575.2	6.1
2009-11-14	19:44:29.36	−22.9595	−66.5863	214.3	6.1	2013-09-25	16:42:43.80	−15.8500	−74.5600	45.8	7.0
2010-02-28	11:25:35.24	−35.0028	−71.5955	41.6	6.2	2013-10-31	23:03:59.30	−30.3000	−71.5600	29.0	6.5
2010-03-04	22:39:25.71	−22.2651	−68.4579	108.4	6.3	2014-03-15	08:59:21.90	−14.0900	−76.3100	20.0	6.1
2010-03-12	16:50:03.80	−34.2768	−71.8879	20.5	5.8	2014-03-15	23:51:33.00	−5.5700	−80.9700	29.0	6.3
2010-03-26	14:52:06.97	−28.0601	−70.9122	41.4	6.1	2014-03-16	21:16:29.60	−19.9800	−70.7000	20.0	6.7
2010-05-02	14:52:42.74	−34.2156	−71.8993	30.3	5.8	2014-03-22	12:59:59.20	−19.7600	−70.8700	20.0	6.2
2010-05-06	02:42:48.46	−18.0961	−70.5865	46.8	6.2	2014-03-23	18:20:01.90	−19.6900	−70.8500	21.0	6.2
2010-05-19	04:15:42.63	−5.1255	−77.4969	129.0	6.0	2014-04-03	01:58:30.50	−20.3100	−70.5800	23.6	6.6
2010-05-23	22:46:51.68	−14.0000	−74.4319	102.6	6.0	2014-04-03	02:43:11.20	−20.5700	−70.5000	10.0	7.7
2010-05-24	16:18:28.81	−8.1152	−71.6412	582.1	6.5	2014-04-04	01:37:50.60	−20.6400	−70.6500	13.7	6.2
2010-07-12	00:11:20.06	−22.2789	−68.3159	109.4	6.1						

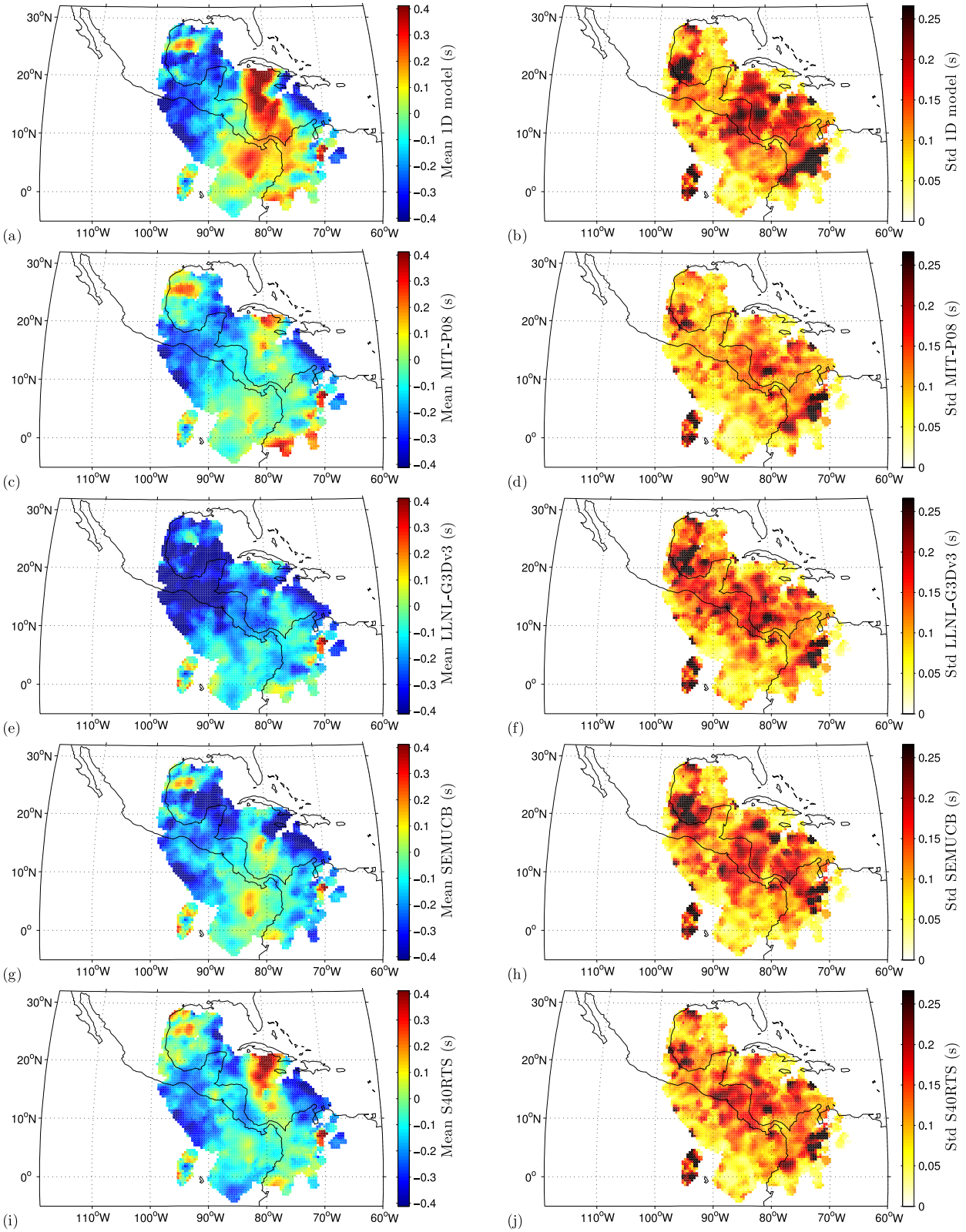

Figure 6. Mean (left column) and standard deviation (right column) of vertical *PcP–P* traveltime residuals averaged over a radius of 0.7° at the CMB with (top) no mantle corrections, and (below) after correcting for mantle structure (from 100 to 2500 km depth) using MIT-P08 (c,d), LLNL-G3Dv3 (e,f), SEMUCB-WM1 (g,h) and S40RTS (i,j) global models.

the traveltime differences and outliers not previously removed. In many locations, the number of events is too small to obtain robust measurements of standard deviation (especially on the borders), and the size of the region used to estimate the mean and the standard deviation is relatively large, a circle of 1.4° of diameter.

Figs 6(c)–(j) show the results after correcting for mantle heterogeneities (from depths of 100 to 2500 km) and the corresponding standard deviations. We find that there is agreement among the four models used for mantle corrections in reducing the band of higher than average traveltimes at about 80°W, resulting in smoother maps with lower than average traveltime anomalies. Therefore, we conclude that this band of high differential traveltimes discussed in previous studies (e.g. Fisher *et al.* 2003; Durand *et al.* 2013) is due to the mantle on the receiver side, for example, waves travelling along the Farallon Plate. The LLNL-G3Dv3 and SEMUCB models produce smoother solutions (Figs 6e and g), while the MIT-P08 and S40RTS models reduce the local standard deviation more (Figs 6d and j). These results agree with Vp and Vs global velocity models that predict higher velocities than average in this region. Global topography models (of much lower resolution) predict a depressed CMB in this area that, if predominant over velocity variations, and taking the CMB reference radius as 2891.5 km (and not shallower), would result in positive traveltime differences. This indicates that, if topography models are correct, one might interpret these maps as due primarily to lateral variations in velocity, with predominantly faster than average velocities. After mantle corrections, the velocity variations are rather uniform over this region: the band of slow traveltime anomalies has disappeared.

5.2 Western Pacific

In this example, we focus on the western border of the Pacific LLSVP, around 10°N–160°W, and also include available data west of this area. Fig. 7 shows the coverage of this region from 50 earthquakes with depth larger than 100 km located along the north Indian plate border (Table 2). We obtained a total of 31 370 high-quality *PcP* observations recorded on short-period stations from Hi-net in Japan. We also excluded seven earthquakes with clear *P* signals but very subtle or undetectable *PcP* signals. To improve the illumination around the border of the LLSVP, we added seven shallower earthquakes.

Figs 8(a) and (b) present local averages of vertical *PcP–P* traveltime differences and their standard deviation with respect to AK135 1-D model. Lateral variations of vertical traveltimes occur at the border of the LLSVP where the sampling is good and the standard deviation is relatively small, but more rapid and stronger variations are present in the western region (about 130°E and 145°E). This is probably due to a strong interaction of the *P* and *PcP* waves sampling the Pacific and Philippine slabs along the Pacific coast and south of Japan in the mid-mantle. When correcting for mantle structure, the *S* models (Figs 8g–j) result in more coherent maps than the *P* models (Figs 8c–f). The *S* models tend to improve standard deviation, while reducing most of the strongest short-wavelength structures (compare Fig. 8a with Figs 8g and i); in contrast, *P*-models somewhat increase standard deviation and show a similar short-wavelength content as the uncorrected map. This behaviour may be due to the higher resolution of upper-mantle *S* models under the oceans compared to *P* models as a result of better coverage.

After correcting for mantle heterogeneity using the two *S* models, the results show a similar trend. They show strong variations at the border of LLSVP, where vertical traveltimes vary about 0.6 s over a distance of 10°, with lower than average traveltimes in the west (outside the LLSVP) of this region. The only exception comes from a few events sampling the CMB in the north of the Philippines showing traveltimes much higher than average. With the current coverage, it is not clear if these results are due to remaining mantle heterogeneities (e.g. from the slabs subducting under Japan) or real D″ structure. The former is likely, since the anomaly is already strongly reduced using current *S* models converted to *P* velocity.

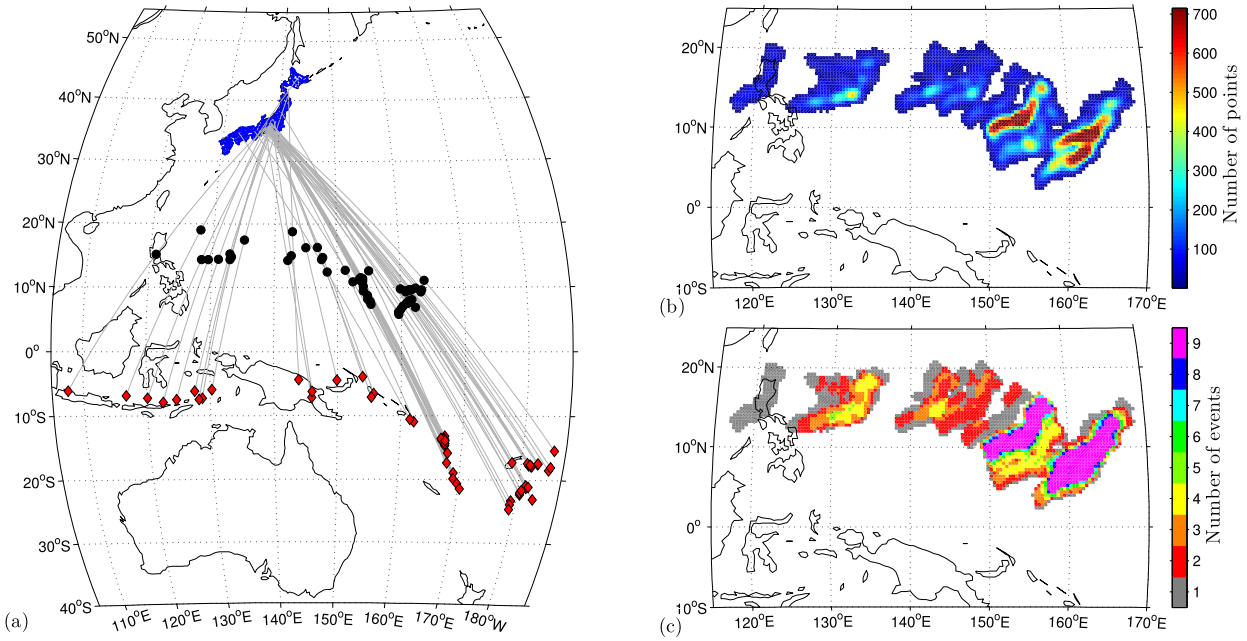

Figure 7. Data set in the western Pacific. (a) Bounce points at the CMB (black circles) for earthquakes along the north Indian plate border (red diamonds) recorded in Japan (blue points). Only bounce points from the centre of the stations of Hi-Net are shown. (b) Number of stations and (c) number of events sampling the CMB averaged over a distance of 0.7°.

Table 2. Event database in the western Pacific from the reviewed ISC bulletin up to December 2012 and from the NEIC global earthquake bulletin afterwards.

Date	Time	Lat (°)	Lon (°)	Depth (km)	M_w	Date	Time	Lat (°)	Lon (°)	Depth (km)	M_w
2004-04-09	15:23:34.45	−13.1691	167.1654	231.1	6.5	2009-11-22	07:48:21.07	−17.8225	−178.3704	526.8	6.4
2004-07-15	04:27:13.33	−17.7045	−178.7667	560.0	7.0	2010-02-15	21:51:48.17	−7.2679	128.7666	134.7	6.2
2004-10-08	08:27:52.42	−10.9373	162.1176	38.0	6.8	2010-03-04	14:02:28.85	−13.6248	167.2326	189.6	6.5
2004-11-05	05:18:33.37	−4.3593	143.9158	120.1	6.0	2010-05-27	17:14:46.93	−13.6734	166.6722	34.7	7.1
2004-11-21	11:07:10.71	−15.3994	−174.8999	238.3	6.0	2010-06-26	05:30:19.80	−10.5716	161.4873	40.3	6.6
2005-02-08	14:48:21.43	−14.3176	167.2603	214.9	6.7	2010-06-30	04:31:01.68	−23.2850	179.1797	572.8	6.3
2005-09-12	21:15:04.24	−17.4748	−177.3684	402.7	5.7	2010-08-16	19:35:48.46	−20.8416	−178.7564	600.8	6.1
2005-10-25	19:40:42.29	−7.1287	145.9402	178.9	5.9	2010-12-13	01:14:42.83	−6.5265	155.6959	144.8	6.1
2006-01-15	11:58:29.16	−7.8818	122.5790	261.7	6.1	2011-02-07	19:53:42.86	−7.0927	155.3183	414.8	6.4
2006-01-23	06:02:59.20	−17.3824	167.7923	33.4	6.3	2011-03-10	17:08:37.32	−6.8567	116.7300	518.6	6.5
2006-02-02	12:48:43.88	−17.8306	−178.2842	599.6	6.7	2011-04-03	14:07:08.98	−17.6066	−178.5336	547.2	6.4
2006-08-07	22:18:55.54	−15.8406	167.8174	148.5	6.8	2011-08-25	10:39:53.63	−13.6631	167.0305	118.4	5.9
2006-09-09	04:13:12.71	−7.2509	120.1277	579.1	6.3	2011-09-03	22:55:35.76	−20.6279	169.7780	136.6	7.0
2006-10-03	18:03:15.12	−18.9296	169.0220	169.2	6.3	2011-09-15	19:31:03.16	−21.5930	−179.3240	629.0	7.3
2007-04-21	17:20:33.39	−13.8949	166.7405	42.7	5.9	2012-03-21	22:15:05.59	−6.2233	146.0083	117.7	6.6
2007-07-23	00:08:32.04	−4.4621	149.8970	560.6	5.9	2012-07-06	02:28:22.55	−14.6567	167.3043	164.8	6.3
2007-08-08	17:04:58.00	−6.0890	107.5839	293.8	7.5	2012-08-05	13:55:10.95	−21.0710	−178.3057	486.3	5.9
2007-08-11	18:04:53.47	−22.2448	−179.5024	607.5	5.6	2012-10-20	23:00:32.93	−13.5730	166.6105	43.5	6.2
2007-11-19	00:52:12.68	−21.2118	−178.6727	558.9	6.3	2012-12-10	16:53:09.49	−6.4969	129.8684	161.5	7.1
2008-01-15	17:52:16.27	−21.9873	−179.5799	597.0	6.5	2012-12-21	22:28:08.08	−14.3591	167.2778	198.1	6.7
2008-04-18	20:39:07.79	−17.3916	−179.0091	556.2	6.3	2013-05-11	20:46:57.60	−17.9700	−175.1100	212.9	6.3
2008-04-29	19:10:02.53	−6.1692	127.5570	404.9	5.9	2013-05-23	17:19:04.80	−23.0100	−177.2300	173.7	7.4
2008-07-19	22:39:52.58	−17.3987	−177.2828	389.2	6.3	2013-06-07	12:54:09.40	−23.8900	179.0900	546.0	5.9
2008-08-04	20:45:15.82	−5.9259	130.3051	188.5	6.1	2013-07-07	18:35:30.70	−3.9200	153.9300	385.5	7.3
2008-09-08	03:03:17.72	−19.8938	169.0874	43.1	6.1	2013-09-01	11:52:29.90	−7.4400	128.2200	112.0	6.5
2008-09-08	18:52:09.04	−13.5186	166.9846	124.7	6.9	2014-01-01	16:03:29.00	−13.8600	167.2500	187.0	6.5
2008-10-22	12:55:57.82	−18.4657	−175.4010	234.8	6.3	2014-05-01	06:36:35.50	−21.4500	170.3500	106.0	6.6
2008-12-06	10:55:27.32	−7.4744	124.6985	406.3	6.4	2014-05-04	09:15:52.90	−24.6100	179.0900	527.0	6.6
2009-11-09	10:44:54.78	−17.2674	178.4528	591.3	7.2						

5.3 Alaska/Canada

Fig. 9 shows the coverage obtained in Alaska and Canada from 50 earthquakes located in northern Pacific and the north polar region (Table 3) with a total of 16 423 high-quality *PcP* observations recorded on broadband stations in North America. In this data set, we exclude events in the Aleutian Islands sampling the gulf of Alaska (south of 55°N and west of 135°W) with epicentral distances shorter than 50°. Along the *P* ray path of these events, global models show strong slow heterogeneities (see the cross-sections in Fig. 3 slightly north of this area). In addition, the 660 discontinuity has strong depth variations (up to 40 km upward deflection) on the source side (Zheng *et al.* 2015). For example, at an epicentral distance of 40°, the separation of the ray paths of *P* and *PcP* at 660 is large (4.72°) which produces a bias of about 5.1 ms km^{-1} (about 0.2 s for a 40 km shallower 660 discontinuity) on *PcP–P* traveltime differences. Even ignoring multipathing effects, these structures have a significant impact on *PcP–P* traveltimes, that cannot be sufficiently reduced with our current mantle corrections and azimuth coverage.

Figs 10(a) and (b) present local means of vertical *PcP–P* traveltime differences and their standard deviation with respect to AK135 1-D model. We observe lower than average traveltimes in the western part of the map that abruptly become much higher than average towards the east, especially in the southern part, around British Columbia, where the standard variation is also the highest. Most of the events sampling this area are located in the Aleutian Islands and epicentral distances range from about 50° to 65°.

Figs 10(c)–(j) show that global models disagree significantly in this region, but they agree on reducing higher than average anomalies. *PcP–P* traveltime results after *P*-model corrections for mantle structure are smoother than using *S* models. When comparing maps corrected using the *P* models (Figs 10c–f), similarly to the example in Central America, the LLNL-G3Dv3 model produces smoother results and the MIT-P08 lower standard deviations. In the *S* models, SEMUCB (Figs 10g–h) reduces the standard deviation in the region about British Columbia while reducing positive anomalies; whereas S40RTS (Figs 10i–j) performs poorly in this region. In our opinion Fig. 10(e) obtains overall the most likely results because it produces the smoothest results (e.g. around British Columbia) while slightly reducing standard deviation in the same region; however, considering the impact of upper-mantle heterogeneities and the discrepancies among these models, it is difficult to judge which of the first three models is best for mantle corrections in this region. A better coverage or, in its absence, the use of 3-D ray-tracing methods and a better upper-mantle model are needed to improve mantle corrections and achieve a more definitive image in this region.

6 DISCUSSION

In Fig. 11, we compare our preferred maps of *PcP–P* traveltime differences projected on the vertical plane after mantle corrections with global tomographic maps of *P* velocity at 2800 km depth obtained using the four mantle models discussed here, and in addition, model HSML-P06 (Houser *et al.* 2008).

When we compare vertical *PcP–P* traveltimes considering the full mantle in the roughest model available, LLNL-G3Dv3, using 1-D ray tracing and 3-D based on pseudo-bending with the LLNL-Earth3D code, we see differences of the order of 0.1 s, and sometimes larger than 0.3 s at short distances. This bias reduces in

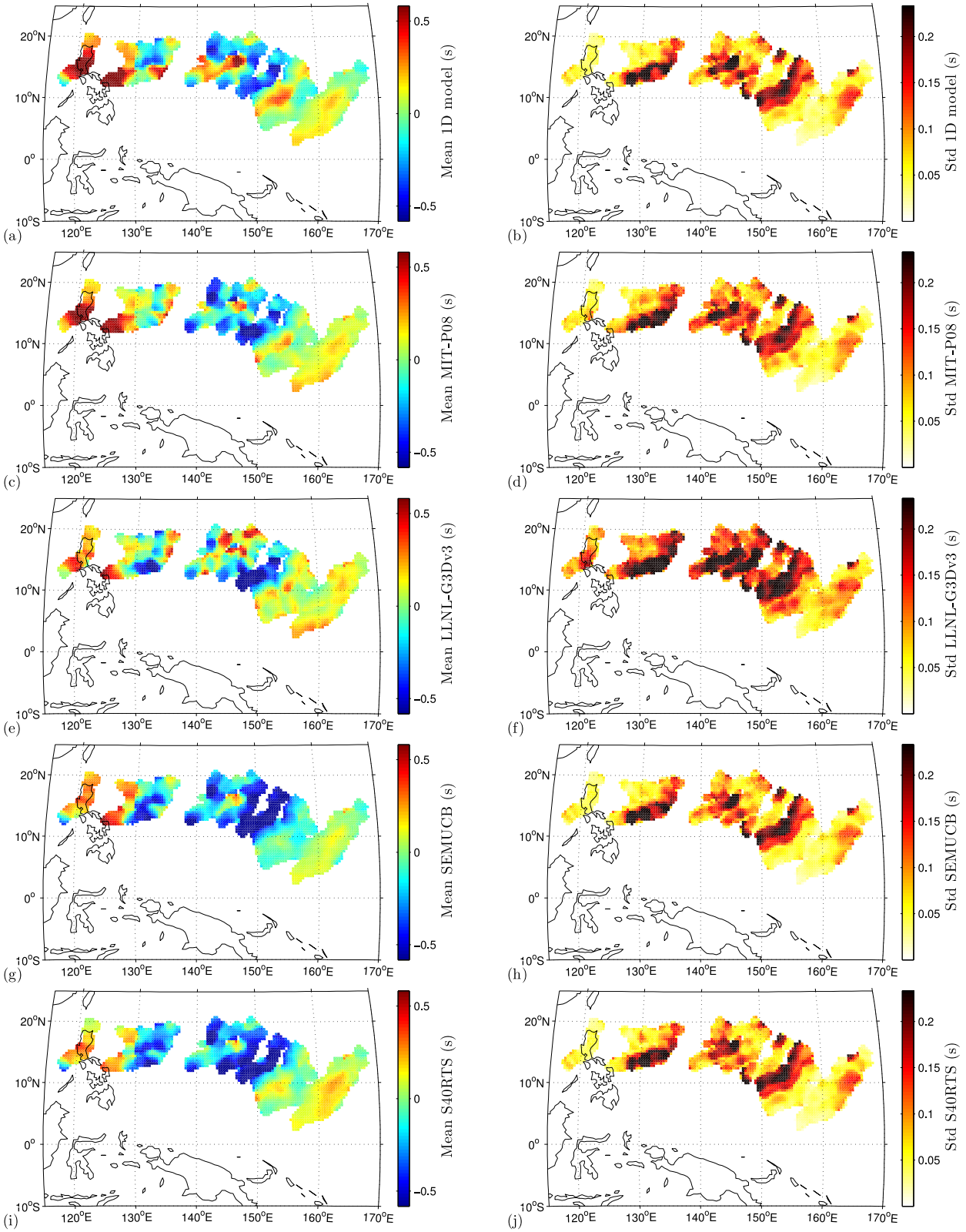

Figure 8. Mean (left column) and standard deviation (right column) of vertical *PcP–P* traveltime anomalies averaged over a radius of 0.7° at the CMB with (a,b) no mantle corrections, and (below) after correcting for mantle structure (from 100 to 2500 km depth) using MIT-P08 (c,d), LLNL-G3Dv3 (e,f), SEMUCB-WM1(g,h) and S40RTS (i,j) global models.

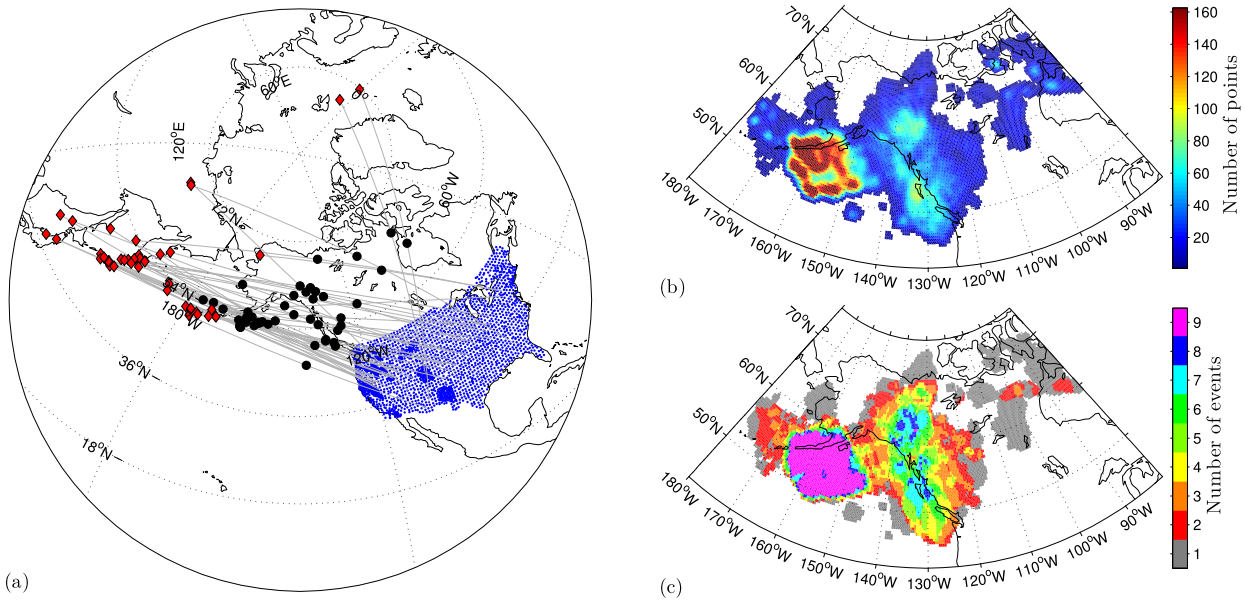

Figure 9. Data set sampling Alaska/western Canada. (a) *PcP* bounce points at the CMB (black circles) from earthquakes in the north Pacific and around the north Pole (red diamonds) recorded at stations in North America (small blue points). Only bounce points from the centre of the stations of USArray are shown. (b) Number of stations and (c) number of events sampling the CMB within a distance of 0.7°.

Table 3. Event database in Alaska/Canada from the reviewed ISC bulletin up to December 2012 and from the NEIC global earthquake bulletin afterwards.

Date	Time	Lat (°)	Lon (°)	Depth (km)	M_w	Date	Time	Lat (°)	Lon (°)	Depth (km)	M_w
2006-08-17	11:11:36.69	55.6643	161.6081	66.0	5.7	2009-12-17	20:01:21.90	51.4385	−179.9962	39.4	5.7
2006-08-24	21:50:37.97	51.1751	157.3980	54.2	6.5	2010-03-30	01:02:54.61	43.2818	138.4944	29.6	5.6
2006-09-16	02:22:50.96	41.3524	135.7497	373.0	5.9	2010-07-18	05:56:45.84	52.7536	−169.7741	21.5	6.6
2006-09-30	17:50:24.44	46.3144	153.1446	20.6	6.6	2010-07-28	11:31:48.26	52.6760	−169.4217	20.3	5.6
2006-10-01	09:06:02.53	46.4670	153.2071	20.7	6.5	2010-07-30	03:56:14.65	52.4218	159.9224	30.3	6.3
2006-10-13	13:47:39.23	46.2897	153.2245	3.2	5.9	2010-09-03	11:16:08.11	51.6273	−176.0005	45.8	6.3
2006-12-07	19:10:22.10	46.1813	154.3750	16.9	6.3	2010-10-08	03:26:14.20	51.3459	−175.3166	24.4	6.2
2007-05-30	20:22:13.56	52.1523	157.2167	122.3	6.4	2010-12-23	14:00:33.45	52.9769	171.1047	26.4	6.2
2007-07-16	01:13:21.88	37.5566	138.4821	7.4	6.5	2011-02-20	21:43:24.88	55.8366	162.2349	39.1	5.9
2007-08-15	20:22:13.00	50.3359	−177.5748	18.9	6.5	2011-08-04	13:51:36.14	48.7670	154.8391	49.8	6.1
2007-09-03	16:14:54.39	45.8019	150.0969	100.6	6.2	2011-10-01	09:23:50.50	51.7171	172.0626	19.1	5.3
2007-10-31	13:44:21.45	51.4950	−178.3970	36.7	5.9	2011-10-25	03:24:50.34	52.1345	−171.8311	49.0	5.6
2008-03-03	09:31:06.69	46.3868	153.1289	36.8	6.3	2012-06-24	03:15:01.98	57.5012	163.4145	16.0	6.0
2008-06-13	23:43:46.79	39.1514	140.7365	11.6	6.8	2012-08-14	02:59:38.86	49.7500	145.3057	590.7	7.7
2008-06-22	23:56:31.03	67.7013	141.1807	22.2	6.1	2012-09-26	23:39:56.50	51.5408	−178.1844	26.8	6.4
2008-07-05	02:12:06.07	53.9462	152.8633	646.1	7.7	2012-11-16	18:12:43.26	49.2365	155.6545	50.8	6.5
2008-07-06	01:00:09.08	45.3251	151.1549	23.2	5.6	2013-02-14	13:13:53.10	67.6300	142.5100	11.0	6.7
2008-07-24	01:43:18.42	50.9283	157.5120	45.3	6.1	2013-02-28	14:05:50.30	50.9700	157.2700	41.0	6.8
2008-08-04	04:42:15.66	49.8638	156.3629	84.0	5.7	2013-03-24	04:18:34.00	50.7300	160.1600	8.0	6.0
2008-09-18	11:58:51.22	51.9447	158.2871	67.3	5.8	2013-04-19	19:58:40.20	49.9700	157.6500	15.0	6.1
2009-01-15	17:49:38.44	46.8333	155.2460	31.1	7.3	2013-04-21	13:48:29.50	51.6600	−178.2400	44.0	5.6
2009-04-07	04:23:34.10	46.0564	151.6371	40.3	6.9	2013-05-19	18:44:10.90	52.3400	160.0700	18.0	5.9
2009-04-18	19:18:01.13	46.0528	151.3971	50.8	6.4	2013-10-01	03:38:21.70	53.2000	152.7900	573.0	6.7
2009-06-22	18:15:40.09	76.3311	6.8091	13.1	5.3	2014-02-26	21:13:40.10	53.6000	−171.8200	265.0	6.1
2009-08-20	06:35:05.24	72.2089	0.9513	9.5	6.0	2014-06-07	04:43:32.50	67.7800	−162.2900	4.0	5.8

smoother models and is not significant on average, but it does have a noticeable effect on the variance. More involved mantle corrections using 3-D ray tracing methods may help to reduce variance and disagreements among mantle models for paths with a strong interaction with slabs, such as in Central America, and may allow us to include observations at relatively short epicentral distances that we now have to reject, such as in Alaska/Canada. Nevertheless, we need higher resolution mantle models to fully correct for these short-scale mantle heterogeneities.

In the regional studies conducted, correcting for mantle heterogeneities from 100 to 2500 km depth improves variance reduction in the data and significantly attenuates fast lateral variations of vertical *PcP–P* traveltimes that are due to contamination by shallow heterogeneities. In Central America, we observe generally higher than average Vp velocity d ln Vp ∼ 0.5 per cent considering a D″ of 250 km thickness and the default CMB depth, with a slight reduction towards the south. In a region where the CMB is found to be depressed, this velocity variation may be higher. In Alaska/Canada,

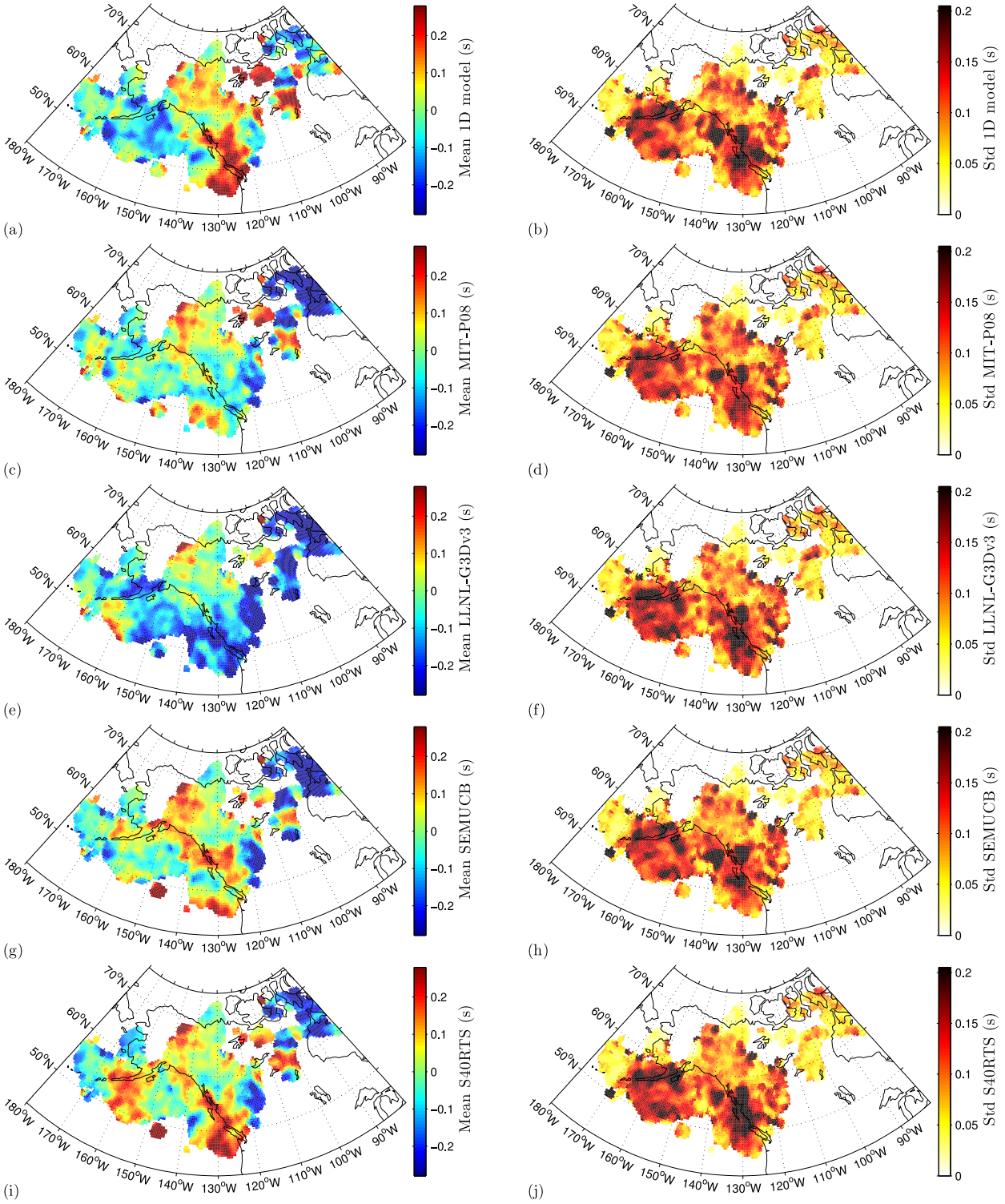

Figure 10. Mean (left column) and standard deviation (right column) of vertical *PcP–P* traveltime anomalies averaged over a radius of 0.7° at the CMB with (top panels) no mantle corrections, and (below) after correcting for mantle (from 100 to 2500 km depth) using MIT-P08 (c,d), LLNL-G3Dv3 (e,f), SEMUCB-WM1 (g,h) and S40RTS (i,j) global models.

we also observe generally higher than average Vp velocity but with stronger lateral variations, results are however less clear than in Central America due to stronger contamination by upper-mantle heterogeneities. In the western Pacific, we observe a Vp velocity reduction of about 1.6 per cent (considering a D″ of 250 km thickness) over a distance of 10° across the western border of the Pacific LLSVP. This reduction may be higher if the CMB is elevated in the LLSVP regions. Note that the fact that the CMB is found depressed in cold/high-velocity regions and elevated in hot/low-velocity buoyant regions (e.g. Lassak *et al.* 2010; Soldati *et al.* 2012) introduces a trade-off between CMB elevation and Vp velocity of about 0.4 per cent d lnVp reduction per kilometer of increased elevation. This

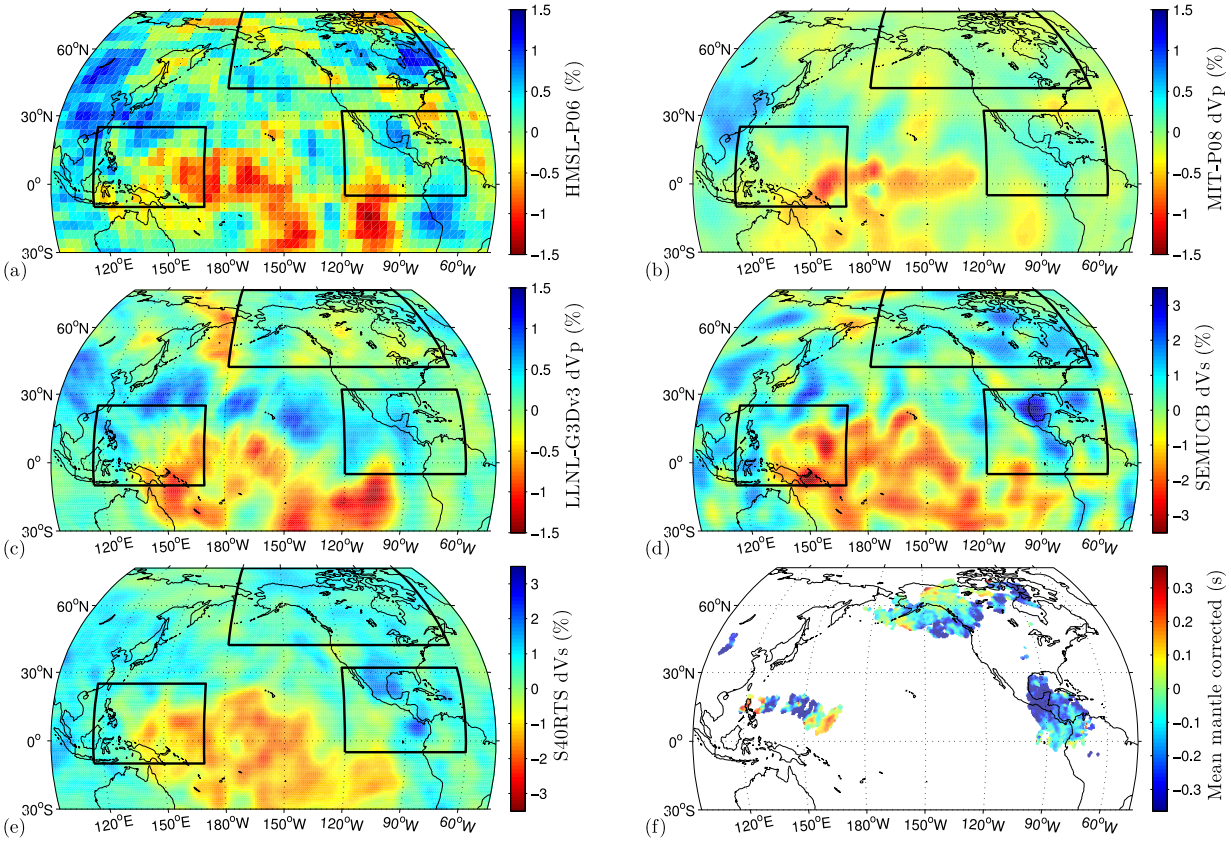

Figure 11. Lateral variations in *P* or *S* velocity at 2800 km depth according to global models: (a) HMSL-P06, (b) MIT-P08, (c) LLNL-G3Dv3, (d) SEMUCB-WM1 and (e) S40RTS compared to (f) the mean of vertical *PcP–P* traveltime differences at the CMB after mantle corrections (the conversion factor from vertical traveltimes to d lnVp is −2.7 per cent per second of traveltime difference, with a D″ thickness of 250 km, and to CMB elevation is −6.8 km s^{-1}). In (a–e), black rectangles delimit the regions considered in this paper.

leads to maximum values of velocity reduction across the western border of the Pacific LLSVP of about 3.6 per cent d lnVp considering a peak-to-peak variation of CMB topography of 5 km, compatible with the lateral Vp velocity variations observed by Tanaka *et al.* (2015) in the same region. The *PcP/P* amplitude ratios (much more sensitive to velocity than elevation) are of help to resolve this trade-off as long as biases due to focusing or attenuation effects are small or can be corrected for.

The study of the weak top D″ reflection (i.e. PdP) may help to better constrain D″ velocity, with the added complication that the topography at the top of D″ may be much stronger than that presently known at the CMB. Many D″ discontinuity detections using SdS are reported in the Central America region from about 140 to 290 km above the CMB. Some of them also report lateral variations of thickness (see, e.g. Kito *et al.* 2007). Few studies using PdP exist in the regions considered, Reasoner & Revenaugh (1999) report a velocity jump of 0.5–0.6 per cent at 190 ± 20 km above the CMB in a region around 90°W in the Pacific. These results are compatible with the velocity variations we see in the same area, about 0.35–0.7 per cent d lnVp considering the same thickness of the D″ region. When we consider a constant velocity of d lnVp ∼ 0.6 per cent, our results translate to variations of D″ thickness in agreement with Thomas *et al.* (2004) using SdS and scattered waves (referred to ScS), namely a shallow D″ discontinuity in the north of this region and deeper in the south. These results are tentative, much more information and accuracy are needed to clearly solve for volumetric structure, topography of the CMB and the D″ discontinuity, and the trade-offs among them.

Overall, there is good agreement among 3-D mantle models after mantle corrections in the three regions considered. At shorter wavelengths, we find no compelling evidence for the lateral variations seen before mantle corrections. The main signals come from the Pacific LLSVP and the ring of fast velocities around the Pacific.

7 CONCLUSIONS

We use dense arrays to illustrate how array processing can dramatically increase the amount of high-quality *PcP* observations, and potentially of much weaker phases. With the slant-stacklet transform, we combine signal from a group of seismometers to attenuate incoherent noise and to separate weak *PcP* signals from stronger signals in the coda of the *P* wave, by exploiting their slowness contrast. Thus, signals that would have been otherwise rejected because of low SNR or high signal interference can still be exploited.

We correct maps of vertical traveltime anomalies in D″ for mantle heterogeneities using several recent *P* and *S* global models. Assuming that a more coherent map indicate better mantle corrections, *P* models achieve the best corrections in Central America and *S* models in the western Pacific. These corrections can be quite significant (as high as 1 s) when *P* and *PcP* kernels sample mantle slabs. Under good azimuthal coverage, mantle heterogeneities should cancel out on average. However, considering the less than ideal coverage of many regions around the globe for this type of measurement, having accurate velocity models of the upper and mid mantle may become more and more important in order to expand

the regions sampled by *PcP–P* and other seismic phases that provide valuable constraints on CMB and the D″ region.

With high-quality *PcP–P* traveltime data obtained using the slant-stacklet approach, we show the importance of mantle corrections on the retrieval of lateral variations of structure at the base of the mantle. While very incomplete in global coverage due to the lack of appropriate arrays, the results are in agreement with results from tomography and other studies. In particular, they allow us to localize the western border of the Pacific LLSVP, albeit only in one place.

The quality and coverage of D″ structure and CMB topography constraints from *PcP–P* traveltime differences may further improve by applying the slant-stacklet transform to exploit complementary information from pPcP-pP or sPcP-sP traveltime differences. Besides, in a scenario where coverage is often extremely limited, further improving corrections for mantle heterogeneities (e.g. using 3-D ray tracing methods or comparing waveforms from real and synthetic seismograms) but also for other sources of bias may prove key for improving our knowledge of the finescale lowermost mantle structure.

Our study also emphasizes the importance of developing high-quality global mantle tomographic models to correct for heterogeneity above D″ and retrieve meaningful maps of lateral variations of seismic structure at the base of the mantle.

In the future, the deployment of (temporary or permanent) dense arrays will provide valuable new observations in many regions around the globe that are currently out of reach. These data combined with *P* diffracted measurements are essential to constrain the scales and amplitudes of lateral variations of structure at the base of the mantle.

ACKNOWLEDGEMENTS

The data used in this work were obtained from the IRIS Data Management Center and NIED DMC. We also acknowledge the support from the European Research Council under the European Community's Seventh Framework Programme (FP7-IDEAS-ERC)/ERC Advanced Grant WAVETOMO.

REFERENCES

Bataille, K. & Lund, F., 1996. Strong scattering of short-period seismic waves by the core-mantle boundary and the P-diffracted wave, *Geophys. Res. Lett.,* **23**(18), 2413–2416.

Bondár, I. & Storchak, D., 2011. Improved location procedures at the International Seismological Centre, *Geophys. J. Int.,* **186**(3), 1220–1244.

Brodholt, J.P., Helffrich, G. & Trampert, J., 2007. Chemical versus thermal heterogeneity in the lower mantle: the most likely role of anelasticity, *Earth planet. Sci. Lett.,* **262**(3–4), 429–437.

Bullen, K.E., 1963. *An Introduction to the Theory of Seismology,* Cambridge Univ. Press.

Cao, A. & Romanowicz, B., 2007. Locating scatterers in the mantle using array analysis of PKP precursors from an earthquake doublet, *Earth planet. Sci. Lett.,* **255**(1–2), 22–31.

Cleary, J.R. & Haddon, R.A.W., 1972. Seismic wave scattering near the core-mantle boundary: a new interpretation of precursors to PKP, *Nature,* **240**(5383), 549–551.

Cobden, L. & Thomas, C., 2013. The origin of D″ reflections: a systematic study of seismic array data sets, *Geophys. J. Int.,* **194**(2), 1091–1118.

Cottaar, S. & Romanowicz, B., 2012. An unsually large ULVZ at the base of the mantle near Hawaii, *Earth planet. Sci. Lett.,* **355–356,** 213–222.

Cottaar, S. & Romanowicz, B., 2013. Observations of changing anisotropy across the southern margin of the African LLSVP, *Geophys. J. Int.,* **195**(2), 1184–1195.

Creager, K.C. & Jordan, T.H., 1986. Aspherical structure of the core-mantle boundary from PKP travel times, *Geophys. Res. Lett.,* **13**(13), 1497–1500.

Durand, S., Matas, J., Ford, S., Ricard, Y., Romanowicz, B. & Montagner, J.-P., 2013. Insights from ScS-S measurements on deep mantle attenuation, *Earth planet. Sci. Lett.,* **374,** 101–110.

Durek, J.J. & Ekström, G., 1995. Evidence of bulk attenuation in the asthenosphere from recordings of the Bolivia Earthquake, *Geophys. Res. Lett.,* **22**(16), 2309–2312.

Dziewonski, A.M., Lekić, V. & Romanowicz, B.A., 2010. Mantle anchor structure: an argument for bottom up tectonics, *Earth Planet. Sci. Lett.,* **299**(1–2), 69–79.

Fisher, J.L., Wysession, M.E. & Fischer, K.M., 2003. Small-scale lateral variations in D″ attenuation and velocity structure, *Geophys. Res. Lett.,* **30**(8), doi:10.1029/2002GL016179.

French, S.W. & Romanowicz, B.A., 2014. Whole-mantle radially anisotropic shear velocity structure from spectral-element waveform tomography, *Geophys. J. Int.,* **199**(3), 1303–1327.

Frost, D.A., Rost, S., Selby, N.D. & Stuart, G.W., 2013. Detection of a tall ridge at the core-mantle boundary from scattered PKP energy, *Geophys. J. Int.,* **195**(1), 558–574.

Garcia, R. & Souriau, A., 2000. Amplitude of the core-mantle boundary topography estimated by stochastic analysis of core phases, *Phys. earth planet. Inter.,* **117**(1–4), 345–359.

Garnero, E.J. & McNamara, A.K., 2008. Structure and dynamics of Earth's lower mantle, *Science,* **320**(5876), 626–628.

Greff-Lefftz, M. & Besse, J., 2012. Paleo movement of continents since 300Ma, mantle dynamics and large wander of the rotational pole, *Earth planet. Sci. Lett.,* **345–348,** 151–158.

Gu, Y.J. & Sacchi, M., 2009. Radon transform methods and their applications in mapping mantle reflectivity structure, *Geophys. Surv.,* **30**(4–5), 327–354.

Hedlin, M.A.H. & Shearer, P.M., 2000. An analysis of large-scale variations in small-scale mantle heterogeneity using Global Seismographic Network recordings of precursors to *PKP*, *J. geophys. Res.,* **105**(B6), 13 655–13 673.

Houser, C., Masters, G., Shearer, P. & Laske, G., 2008. Shear and compressional velocity models of the mantle from cluster analysis of long-period waveforms, *Geophys. J. Int.,* **174**(1), 195–212.

Ishii, M. & Tromp, J., 1999. Normal-mode and free-air gravity constraints on lateral variations in velocity and density of Earth's mantle, *Science,* **285**(5431), 1231–1236.

Ishii, M. & Tromp, J., 2004. Constraining large-scale mantle heterogeneity using mantle and inner-core sensitive normal modes, *Phys. earth planet. Inter.,* **146**(1–2), 113–124.

Jensen, K.J., Thorne, M.S. & Rost, S., 2013. SPdKS analysis of ultralow-velocity zones beneath the western Pacific, *Geophys. Res. Lett.,* **40**(17), 4574–4578.

Julian, B. & Gubbins, D., 1977. Three-dimensional seismic ray tracing, *J. geophys. Res.,* **43**(1), 95–114.

Kawai, K., Takeuchi, N. & Geller, R.J., 2006. Complete synthetic seismograms up to 2 Hz for transversely isotropic spherically symmetric media, *Geophys. J. Int.,* **164,** 411–424.

Kito, T., Rost, S., Thomas, C. & Garnero, E.J., 2007. New insights into the P- and S-wave velocity structure of the D″ discontinuity beneath the Cocos plate, *Geophys. J. Int.,* **169**(2), 631–645.

Lassak, T.M., McNamara, A.K., Garnero, E.J. & Zhong, S., 2010. Core–mantle boundary topography as a possible constraint on lower mantle chemistry and dynamics, *Earth planet. Sci. Lett.,* **289**(1–2), 232–241.

Lay, T., 2015. Deep Earth structure – lower mantle and D″, in *Treatise on Geophysics,* Vol. 1, 2nd edn, Elsevier, pp. 683–723.

Lay, T. & Garnero, E.J., 2011. Deep mantle seismic modeling and imaging, *Ann. Rev. Earth planet Sci.,* **39**(1), 91–123.

Lay, T. & Helmberger, D.V., 1983a. A lower mantle S-wave triplication and the shear velocity structure of D″, *Geophys. J. Int.,* **75**(3), 799–837.

Lay, T. & Helmberger, D.V., 1983b. A shear velocity discontinuity in the lower mantle, *Geophys. Res. Lett.,* **10**(1), 63–66.

Lekic, V., Cottaar, S., Dziewonski, A. & Romanowicz, B., 2012. Cluster analysis of global lower mantle tomography: a new class of structure and implications for chemical heterogeneity, *Earth planet. Sci. Lett.,* **357–358,** 68–77.

Li, J., Stoica, P. & Wang, Z., 2003. On robust Capon beamforming and diagonal loading, *IEEE Trans. Signal Process.,* **51**(7), 1702–1715.

Li, C., van der Hilst, R.D., Engdahl, E.R. & Burdick, S., 2008. A new global model for P wave speed variations in Earth's mantle, *Geochem. Geophys. Geosyst.,* **9**(5), Q05018, doi:10.1029/2007GC001806.

Lorenz, R. & Boyd, S., 2005. Robust minimum variance beamforming, *IEEE Trans. Signal Process.,* **53**(5), 1684–1696.

Lynner, C. & Long, M.D., 2014. Lowermost mantle anisotropy and deformation along the boundary of the African LLSVP, *Geophys. Res. Lett.,* **41**(10), 3447–3454.

Margerin, L., 2003. Multiple scattering of high-frequency seismic waves in the deep Earth: PKP precursor analysis and inversion for mantle granularity, *J. geophys. Res.,* **108**(B11), doi:10.1029/2003JB002455.

Masters, G., Laske, G., Bolton, H. & Dziewonski, A., 2000. *Earth–Deep Interior: Mineral Physics and Tomography From the Atomic to the Global Scale,* vol. 117 of Geophysical Monograph, pp. 63–87, American Geophysical Union.

McNamara, A.K., Garnero, E.J. & Rost, S., 2010. Tracking deep mantle reservoirs with ultra-low velocity zones, *Earth Planet. Sci. Lett.,* **299**(1–2), 1–9.

Morelli, A. & Dziewonski, A.M., 1987. Topography of the core-mantle boundary and lateral homogeneity of the liquid core, *Nature,* **325**(6106), 678–683.

Moser, T., 1991. Shortest path calculation of seismic rays, *Geophysics,* **56**(1), 59–67.

Ni, S. & Helmberger, D.V., 2001. Probing an ultra-low velocity zone at the core mantle boundary with P and S waves, *Geophys. Res. Lett.,* **28**(12), 2345–2348.

Nissen-Meyer, T., van Driel, M., Stähler, S.C., Hosseini, K., Hempel, S., Auer, L., Colombi, A. & Fournier, A., 2014. AxiSEM: broadband 3-D seismic wavefields in axisymmetric media, *Solid Earth,* **5**(1), 425–445.

Obara, K., Kasahara, K., Hori, S. & Okada, Y., 2005. A densely distributed high-sensitivity seismograph network in Japan: Hi-net by National Research Institute for Earth Science and Disaster Prevention, *Rev. Sci. Instrum.,* **76**(2), 021301, doi:10.1063/1.1854197.

Okada, Y., Kasahara, K., Hori, S., Obara, K., Sekiguchi, S., Fujiwara, H. & Yamamoto, A., 2004. Recent progress of seismic observation networks in Japan – Hi-net, F-net, K-NET and KiK-net–, *Earth planet. Space,* **56**(8), xv–xxviii.

Reasoner, C. & Revenaugh, J., 1999. Short-period P wave constraints on D″ reflectivity, *J. geophys. Res.,* **104**(B1), 955–962.

Ritsema, J. & van Heijst, H.-J., 2002. Constraints on the correlation of P- and S-wave velocity heterogeneity in the mantle from P, PP, PPP and PKPab traveltimes, *Geophys. J. Int.,* **149**(2), 482–489.

Ritsema, J., Deuss, A., van Heijst, H.J. & Woodhouse, J.H., 2011. S40RTS: a degree-40 shear-velocity model for the mantle from new Rayleigh wave dispersion, teleseismic traveltime and normal-mode splitting function measurements, *Geophys. J. Int.,* **184**(3), 1223–1236.

Rodgers, A. & Wahr, J., 1993. Inference of core-mantle boundary topography from ISC PcP and PKP traveltimes, *Geophys. J. Int.,* **115**(3), 991–1011.

Romanowicz, B., 2001. Can we resolve 3D density heterogeneity in the lower mantle?, *Geophys. Res. Lett.,* **28**(6), 1107–1110.

Rost, S. & Thomas, C., 2010. High resolution CMB imaging from migration of short-period core reflected phases, *Phys. Earth Planet. Inter.,* **183**(1–2), 143–150.

Roy, S.K., Ravi Kumar, M. & Srinagesh, D., 2014. Upper and lower mantle anisotropy inferred from comprehensive SKS and SKKS splitting measurements from India, *Earth planet. Sci. Lett.,* **392,** 192–206.

Samuel, H., Farnetani, C.G. & Andrault, D., 2005. *Earth's Deep Mantle: Structure, Composition, and Evolution,* vol. 160 of Geophysical Monograph, pp. 101–116, American Geophysical Union.

Schimmel, M. & Gallart, J., 2003. The use of instantaneous polarization attributes for seismic signal detection and image enhancement, *Geophys. J. Int.,* **155**(2), 653–668.

Schimmel, M. & Gallart, J., 2004. Degree of polarization filter for frequency-dependent signal enhancement through noise suppression, *Bull. seism. Soc. Am.,* **94**(3), 1016–1035.

Schimmel, M. & Gallart, J., 2007. Frequency-dependent phase coherence for noise suppression in seismic array data, *J. geophys. Res.,* **112,** B04303, doi:10.1029/2006JB004680.

Schimmel, M. & Paulssen, H., 1997. Noise reduction and detection of weak, coherent signals through phase-weighted stacks, *Geophys. J. Int.,* **130**(2), 497–505.

Simmons, N.A., Myers, S.C., Johannesson, G. & Matzel, E., 2012. LLNL-G3Dv3: global *P* wave tomography model for improved regional and teleseismic traveltime prediction, *J. geophys. Res.,* **117,** B10302, doi:10.1029/2012JB009525.

Soldati, G., Boschi, L. & Forte, A.M., 2012. Tomography of core-mantle boundary and lowermost mantle coupled by geodynamics, *Geophys. J. Int.,* **189**(2), 730–746.

Soldati, G., Koelemeijer, P., Boschi, L. & Deuss, A., 2013. Constraints on core-mantle boundary topography from normal mode splitting, *Geochem. Geophys. Geosyst.,* **14**(5), 1333–1342.

Sylvander, M., Ponce, B. & Souriau, A., 1997. Seismic velocities at the core-mantle boundary inferred from P waves diffracted around the core, *Phys. Earth planet. Inter.,* **101**(3–4), 189–202.

Sze, E.K. & van der Hilst, R.D., 2003. Core mantle boundary topography from short period PcP, PKP, and PKKP data, *Phys. Earth planet. Inter.,* **135**(1), 27–46.

Tanaka, S., Kawakatsu, H., Obayashi, M., Chen, Y.J., Ning, J., Grand, S.P., Niu, F. & Ni, J., 2015. Rapid lateral variation of P-wave velocity at the base of the mantle near the edge of the Large-Low Shear Velocity Province beneath the western Pacific, *Geophys. J. Int.,* **200**(2), 1052–1065.

Taner, M.T., Koehler, F. & Sheriff, R.E., 1979. Complex seismic trace analysis, *Geophysics,* **44**(6), 1041–1063.

Thomas, C. & Laske, G., 2015. D″ observations in the Pacific from PLUME ocean bottom seismometer recordings, *Geophys. J. Int.,* **200**(2), 849–860.

Thomas, C., Heesom, T. & Kendall, J.M., 2002. Investigating the heterogeneity of the D″ region beneath the northern Pacific using a seismic array, *J. geophys. Res.,* **107**(B11), ESE 3–1–ESE 3–7.

Thomas, C., Garnero, E.J. & Lay, T., 2004. High-resolution imaging of lowermost mantle structure under the Cocos plate, *J. geophys. Res.,* **109,** B8307, doi:10.1029/2004JB003013.

Thorne, M.S., Garnero, E.J., Jahnke, G., Igel, H. & McNamara, A.K., 2013. Mega ultra low velocity zone and mantle flow, *Earth planet. Sci. Lett.,* **364,** 59–67.

Tkalčić, H., Romanowicz, B. & Houy, N., 2002. Constraints on D″ structure using PKP(AB-DF), PKP(BC-DF) and PcP–P traveltime data from broadband records, *Geophys. J. Int.,* **149**(3), 599–616.

To, A., Romanowicz, B., Capdeville, Y. & Takeuchi, N., 2005. 3D effects of sharp boundaries at the borders of the (African) and (Pacific) superplumes: observation and modeling, *Earth planet. Sci. Lett.,* **233**(1–2), 137–153.

Torsvik, T., Steinberger, B., Cocks, L. & Burke, K., 2008. Longitude: Linking Earth's ancient surface to its deep interior, *Earth planet. Sci. Lett.,* **276**(3–4), 273–282.

Valenzuela, R.W. & Wysession, M.E., 1998. Illuminating the base of the mantle with diffracted waves, *The Core–Mantle Boundary Region,* pp. 57–71, doi:10.1029/GD028p0057.

van der Hilst, R.D., de Hoop, M.V., Wang, P., Shim, S.-H., Ma, P. & Tenorio, L., 2007. Seismostratigraphy and thermal structure of Earth's core-mantle boundary region, *Science,* **315**(5820), 1813–1817.

Ventosa, S. & Romanowicz, B., 2015. Extraction of weak PcP phases using the slant-stacklet transform – I: method and examples, *Geophys. J. Int.,* **201**(1), 207–223.

Vidale, J.E. & Hedlin, M.A.H., 1998. Evidence for partial melt at the core-mantle boundary north of Tonga from the strong scattering of seismic waves, *Nature,* **391**(6668), 682–685.

Vinnik, L.P., Farra, V. & Romanowicz, B., 1989. Observational evidence for diffracted SV in the shadow of the Earth's core, *Geophys. Res. Lett.,* **16**(6), 519–522.

Wysession, M.E., 1996. Large-scale structure at the core-mantle boundary from diffracted waves, *Nature,* **382**(6588), 244–248.

Wysession, M.E., Lay, T., Revenaugh, J., Williams, Q., Garnero, E.J., Jeanloz, R. & Kellogg, L.H., 1998. The D″ discontinuity and its implications, in *The Core-Mantle Boundary Region,* pp. 273–297, eds Gurnis, M., Wysession, M.E., Knittle, E. & Buffett, B.A., American Geophysical Union.

Young, M.K., Tkalčić, H., Bodin, T. & Sambridge, M., 2013. Global P wave tomography of Earth's lowermost mantle from partition modeling, *J. geophys. Res.,* **118**(10), 5467–5486.

Zhao, D., Hasegawa, A. & Horiuchi, S., 1992. Tomographic imaging of *P* and *S* wave velocity structure beneath northeastern Japan, *J. geophys. Res.,* **97**(B13), 19 909–19 928.

Zheng, Z., Ventosa, S. & Romanowicz, B., 2015. High resolution upper mantle discontinuity images across the Pacific Ocean from SS precursors using local slant stack filters, *Geophys. J. Int.,* **202**(1), 175–189.

APPENDIX: EXAMPLE ON THE BIAS DUE TO UPPER-MANTLE HETEROGENEITIES AND DISCONTINUITY TOPOGRAPHY

The bias on the *PcP* arrival time due to variations in the Moho depth at an epicentral distance of 60°, according to the PREM model, is about 24.5 ms km^{-1}, and about 4.8 ms km^{-1} at the 670 discontinuity; while 1 per cent increase on Vp at 400 km produces a bias of about 1.2 ms km^{-1}. Absolute *PcP* arrival times are then primarily affected by shallow heterogeneities, while differential *PcP–P* traveltimes will be more affected by the deeper upper mantle. For epicentral distances of 70° (Fig. A1), the separation of the ray paths of *P* and *PcP* is approximately equal to the Fresnel zone radius at 2 s at a depth of 500 km and reduces to about 100 km for epicentral distances of 40°. As a consequence, the Fresnel volumes of *P* and *PcP* mostly overlap at the Moho and any velocity and topography discrepancy between the regions sampled by *P* and *PcP* is greatly attenuated. However, they do not overlap in the transition zone for short epicentral distances or short wavelengths. Considering that at least those heterogeneities that are known are significantly larger than 2°, this implies in practice that the gradient of lateral variations at the borders and within a heterogeneity is more important than its absolute perturbation with respect to a reference 1-D model. For example, variations in the Moho depth at a distance of 60° produce bias of about 2.1 ms km^{-1} on *PcP–P* traveltime differences due to the large overlap between the *P* and *PcP* kernels. At a depth of 670 km the separation of the ray paths of *P* and *PcP* increases up to 234 km (2.35°) while the Fresnel zone radii increase only up to 113 and 105 km, respectively. Therefore the bias on the *PcP–P* traveltime in case of a deeper 670 discontinuity is about 1.5 ms km^{-1}, whereas a gradient at 670 of 1 km deg^{-1} produces a bias of about 15 ms (*P* seeing a deeper discontinuity than *PcP*). Similarly, a 1 per cent increase in Vp at 400 km produces a bias of about 0.2 ms km^{-1}, and 1.5 ms if the gradient is 1 km deg^{-1}.

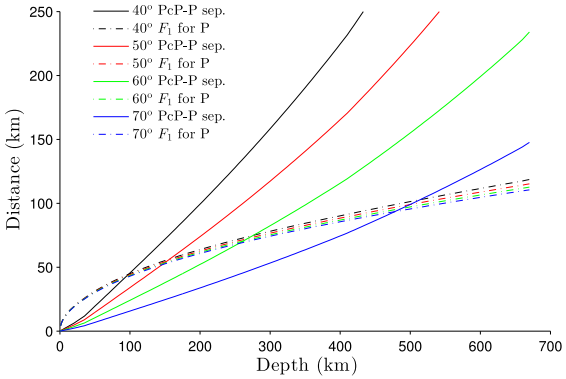

Figure A1. Separation between *P* and *PcP* ray paths as a function of depth using the AK135 1-D model compared to the Fresnel zone radius of the *P* wave for a period of 2 s. The radius of *PcP* is slightly lower than the *P* radius.